JPhys Photonics

TOPICAL REVIEW • OPEN ACCESS

High power, high repetition rate laser-based sources for attosecond science

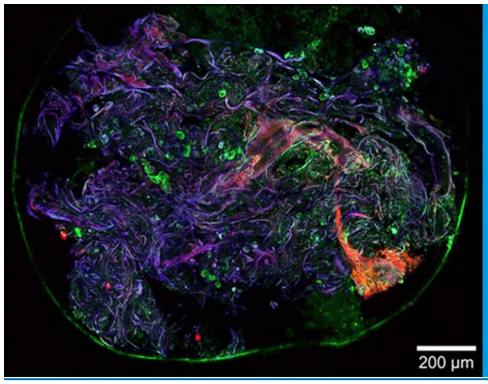

Journal of Physics: Photonics

OPEN ACCESS

RECEIVED
9 February 2022

REVISED
26 April 2022

ACCEPTED FOR PUBLICATION
31 May 2022

PUBLISHED
14 June 2022

TOPICAL REVIEW

High power, high repetition rate laser-based sources for attosecond science

F J Furch*, T Witting, M Osolodkov, F Schell, C P Schulz and M J J Vrakking

Max-Born-Institut für Nichtlineare Optik und Kurzzeit Spektroskopie, Berlin, Germany
* Author to whom any correspondence should be addressed.

E-mail: furch@mbi-berlin.de

Keywords: ultrafast optics, attosecond science, high repetition rate, OPCPA, nonlinear pulse compression, few-cycle pulses

Abstract

Within the last two decades attosecond science has been established as a novel research field providing insights into the ultrafast electron dynamics that follows a photoexcitation or photoionization process. Enabled by technological advances in ultrafast laser amplifiers, attosecond science has been in turn, a powerful engine driving the development of novel sources of intense ultrafast laser pulses. This article focuses on the development of high repetition rate laser-based sources delivering high energy pulses with a duration of only a few optical cycles, for applications in attosecond science. In particular, a high power, high repetition rate optical parametric chirped pulse amplification system is described, which was developed to drive an attosecond pump-probe beamline targeting photoionization experiments with electron-ion coincidence detection at high acquisition rates.

1. Introduction

Ultrashort laser pulses have enabled many exciting fields of research. Short pulse durations in the ps- and fs-range provide access to time-resolved studies on timescales not accessible otherwise and, when combined with high pulse energies, states of matter with unique properties can be produced and probed. Some notable examples include the study of ultrafast magnetization dynamics [1], dense plasma dynamics [2], laser material processing [3], laser surgery [4], femtochemistry [5] and precision spectroscopy [6] among many others. Ultrashort laser pulses have also enabled the generation of sub-femtosecond pulses in the extreme ultraviolet (XUV) region of the electromagnetic spectrum opening the door for the study of ultrafast processes on few-femtosecond and sub-femtosecond (i.e. attosecond) timescales. In this article the attention is centered around the field of attosecond science, which studies the fastest processes produced in a laboratory to date. In particular, the article focuses around some of the latest developments in sources of intense, ultrashort laser pulses with high repetition rate enabling new avenues in attosecond science.

1.1. Attosecond science

The characteristic timescale for the motion of electrons in atoms, molecules and solids ranges from tens of femtoseconds (1 fs $= 10^{-15}$ s) down to a few tens of attoseconds (1 as $= 10^{-18}$ s), governed by the energy separation between different electronic states. The study of electron dynamics on these ultrashort timescales is the realm of attosecond science [7]. More precisely, attosecond science studies the ultrafast electron dynamics that follows a photoionization or photoexcitation process.

Time-resolved studies with sub-femtosecond resolution have been realized in experiments driven by femtosecond laser pulses in the visible (VIS) or infrared (IR) region of the electromagnetic spectrum [8–11]. However, the core of the work in attosecond science is based on pump-probe studies driven by pulses in the XUV with durations between a few tens and a few hundreds of attoseconds. Moreover, given that until recently [12, 13] the photon flux in sources of attosecond pulses was not sufficient to drive an XUV-pump-XUV-probe experiment, the attosecond pulses are typically combined with phase-locked pulses in the IR, where the optical cycle of the IR acts as a clock with attosecond time resolution. In most of these

XUV-IR pump-probe experiments, the XUV attosecond pulse acts as a trigger, launching a rapidly evolving electron wave-packet by means of a sudden photoionization or photoexcitation event. Meanwhile, the electric field of the IR pulse provides a temporal gradient capable of probing the evolution of the electronic wave-packet with a time resolution that is well below the duration of the IR optical cycle. The observables in these experiments are typically the kinetic energy or momentum distribution of photoions or photoelectrons generated during the light–matter interaction, or the XUV-IR delay-dependent absorption of the XUV pulse (Attosecond Transient Absorption Spectroscopy or ATAS). These experiments have provided unprecedented insight into the ultrafast electron dynamics in atoms, molecules and solids. Some outstanding examples include observation of the temporal evolution of an Auger decay [14], the real time observation of light-induced electron tunneling in atoms [15], control of the localization of an electron in a molecule undergoing dissociation [16], and the characterization of a photoelectron wave packet created through an autoionizing resonance [17]. In the former examples, the experimental observables were the kinetic energy or momentum distributions of photoelectrons or photoions produced during photoionization. In ATAS the configuration of the experiment is slightly different: a strong IR or VIS pulse is used to excite the system and the spectrally resolved absorption of the XUV pulse is utilized to probe the evolution of the system. This technique has been successfully implemented for example, to observe valence electron motion in an atom in real time [18], to observe the buildup of a Fano resonance in real time [19], to study the state-resolved evolution of the induced dipole response in a molecule [20], and to explore the ultrafast electronic response of a dielectric material to a strong laser [21].

1.2. Attosecond pulses

Coherent light pulses with durations in the attosecond range represent the key technological enabler for attosecond science. The XUV pulses are typically produced through the well-known process of high-order harmonic generation (HHG) [22, 23], which takes place when intense VIS or IR laser pulses interact with, most commonly, a noble gas. HHG can be described according to a simple and intuitive model [24, 25]. At the atomic level the strong laser field distorts the Coulomb potential and induces tunnel ionization. Subsequently, the free electron is accelerated in the oscillating laser field and recollides with the parent ion. Upon recombination, the ionization energy (IP) of the atom plus the kinetic energy gained by the electron in the electric field of the laser, are converted to high energy photons that reach well into the XUV region of the electromagnetic spectrum. The process is repeated every half-cycle of the IR laser pulse and naturally leads to the emission of a train of sub-femtosecond pulses in the time domain [26]. In the frequency domain, this implies that the XUV frequencies are odd multiples of the IR laser fundamental frequency. In addition, phase matching conditions ensuring that atoms emit in phase with the propagating XUV field, have to be met in order to generate an observable photon flux [27, 28].

The ionization process is confined to a short time window within the IR laser half-cycle during which the electric field is sufficiently strong. For example, for an 800 nm laser the half-cycle duration is approximately 1.35 fs and therefore ionization occurs on an attosecond timescale. Similarly, the recollision/recombination step also happens in a short window within the laser half-cycle. As a result, the emitted XUV pulses have a duration in the attosecond range. Moreover, when the spectral phase acquired during the generation process is compensated [29, 30], the duration of these attosecond pulses can be shortened and can approach the Fourier-transform limit.

Attosecond pulse trains (APTs) in combination with synchronized IR pulses have been utilized in numerous experiments and provide access to attosecond time resolution in studies of ultrafast electron dynamics. Some examples from the literature include the determination of photoionization time delays between photoelectrons originating from different states of an atom [31], or the study of the time-dependent dipole induced in a small molecule by the near-IR (NIR) field [32]. In this type of experiment, the APT triggers a particular process (e.g.: it launches a photolectron wave packet in the continuum) multiple times at regular time intervals, leading inherently to a quantum interference process. However, for the observation of many processes occurring during, or immediately after the light–matter interaction, it is often necessary that the process to be studied is triggered only a single time. In that case, the XUV emission must be confined to a single event. As a matter of fact, as the duration of the IR pulse driving the HHG process is shortened, the number of half-cycles within the laser pulse in which the electric field is strong enough to induce the necessary ionization plus recombination process decreases. When harmonic generation is driven by laser pulses lasting only a few optical cycles, one of several existing temporal gating methods can be used to confine the harmonic emission to a single half-cycle of the driving laser pulse and produce isolated attosecond pulses (IAPs). For example, given that the cutoff frequency for the harmonic emission depends on the driving laser intensity through the ponderomotive potential U_p as [33]:

$$h\nu_{max} = \mathrm{IP} + 3.17\, U_p \tag{1}$$

where ν_{max} is the maximum or cutoff frequency, h is Planck's constant and IP is the ionization potential of the atoms in the gas, only the most intense part of the driving pulse will contribute to the generation of XUV light in the cutoff region of the spectrum. For a driving pulse lasting only a few optical cycles, the generation of cutoff harmonics is naturally confined to one or two IR half-cycles depending on the value of the carrier-envelope phase (CEP) [34]. In 2004 Kienberger *et al* combined spectral filtering of the XUV emission with control of the CEP (amplitude gating) to generate IAPs [35]. Another extended method to produce IAPs consists of modulating the polarization of the few-cycle IR pulse in time, such that the driving pulse possesses linear polarization (and is able to generate harmonics only) during a short time window of around one half cycle (polarization gating) [36–39]. Other known methods include the use of two-color fields [40–42], control of the ionization level of the medium during the leading edge of the pulse (intensity gating) [43], and the generation of harmonics with variable emission direction exploiting linear space-time couplings in the few-cycle driver (attosecond light house effect) [44]. Note that except for a few exceptions [45], generating IAPs requires few-cycle pulses and control over the waveform of the driving laser pulse during HHG, via control of the CEP.

Ti:Sapphire chirped pulse amplification (CPA) systems provide an ideal source of NIR pulses for driving the HHG process and attosecond pump-probe experiments. Sub-50 fs pulses with energies ranging from a few hundred μJ to a few mJ are routinely utilized in laboratories around the world to generate APTs. Moreover, in order to generate IAPs, the CEP of the amplified pulses can be controlled with commercially available devices and the NIR pulse duration can be shortened down to only a few optical cycles (usually $<$5 fs; i.e. $<$2 optical cycles at a central wavelength of 800 nm), by spectral broadening in a gas-filled hollow-core fiber [46] followed by spectral phase compensation with chirped mirrors.

1.3. Beyond Ti:Sapphire systems: high repetition rate systems

Ti:Sapphire CPAs with the pulse characteristics previously described operate at repetition rates of a few kHz. However, for some applications it is important to implement higher repetition rates. In the context of gas-phase experiments in attosecond science with atomic and molecular targets, it is extremely attractive to detect all charged particles produced during photoionization in coincidence. Detection in coincidence means that for each detection event, all detected charged particles can be correlated to a single ionization event; i.e. it is possible to discern which electron(s) and which ion(s) originated from the same parent atom or molecule. Measurement of fully correlated three-dimensional momentum vectors of all charged particles in coincidence can be realized in a reaction microscope (ReMi), also known as COLTRIMS machine: COLd Target Recoil-Ion Momentum Spectroscopy [47]. In experiments involving molecular targets, detection in coincidence allows retrieving photoelectron momentum distributions correlated to particular molecular fragments, or the photoelectron angular distribution in the recoil frame of a dissociating molecule. In the complex scenarios that arise during attosecond pump-probe experiments, involving non-perturbative excitations of multiple energy levels, multi-electron correlations, and coupling between electronic and nuclear degrees of freedom, access to many correlated observables in a single experiment is extremely attractive.

Detection in coincidence naturally requires that only one photoionization event is produced during the interaction between the laser pulses and the target. Ionization of multiple atoms/molecules coupled to realistic detection efficiencies ($<$1) would lead to electrons and ions from different parent atoms/molecules being falsely identified as correlated (false coincidence). In practice, a maximum ionization rate of approximately 20% of the laser repetition rate ensures a low incidence of false coincidences [48–50]. This upper limit to the ionization rate implies a strong demand on the repetition rate of the laser source driving the experiment, if an experiment is to be completed within a reasonable time or to make the experiment even feasible. For example, if one considers studying a particular dissociation channel of a molecule that takes place with a probability of 0.1 (given photoionization at a particular photon energy), at an ionization rate of 0.2 of the laser repetition rate, then required events would occur at a rate of 0.02 times the laser repetition rate. If in addition one requires acquiring 10^6 events where the dissociation takes place in order to build up reasonable statistics, that would translate into measuring for almost 14 h for a laser operating at 1 kHz (with perfect detection efficiencies). But in a typical pump-probe experiment the measurement has to be repeated for several tens of different pump-probe delays, extending the measuring time to several weeks, during which all conditions in the laboratory have to remain stable. The introduction of coincidence detection in attosecond pump-probe experiments has been made possible by Ti:Sapphire CPAs running at 10 kHz [51]. The potential of the technique is illustrated by some remarkable experiments in small molecular systems [52, 53]. However, more complex problems, involving the study of low probability ionization channels, require higher repetition rates.

Time-resolved surface photoemission is another area within attosecond science where high repetition rate sources introduce a significant advantage. In this case, the number of photoelectrons per laser pulse

generated from a surface or a nano-structure has to be kept small in order to avoid degradation of the photoelectron momentum resolution due to space-charge effects. Notable examples are the study of nanoplasmonic dynamics by energy-resolved photoelectron emission microscopy [54] or the study of delays in photoemission from metal surfaces [55].

During the last several years much of the efforts in ultrafast laser development have been devoted to increasing the average power and repetition rate of these sources, for the benefit of many different applications. Optical parametric chirped pulse amplification (OPCPA) systems pumped by high-power, high-repetition rate CPAs have been identified long ago as an alternative to traditional Ti:Sapphire CPAs for driving attosecond pump-probe experiments at much higher repetition rates [56, 57]. Moreover, in the last few years, the direct nonlinear post-compression of laser pulses from high-power, high-repetition rate CPAs based on Yb-doped materials, has emerged as a valuable alternative to OPCPAs [58]. In the following section we will review the main characteristics of these two techniques and introduce the high-power, high-repetition rate OPCPA developed at the Max-Born-Institute for driving attosecond pump-probe experiments with coincidence detection.

2. High power, high repetition rate sources

The development of sources of ultrashort laser pulses with high peak and average power and high repetition rate has been a major focus of attention both in the academic and industrial sectors, for more than ten years now. Arguably the main two components enabling this technology are Yb-doped laser gain materials, and high-power laser diodes with emission wavelengths resonant with the absorption bands of these laser gain materials. The low quantum defect, excellent thermo-mechanical properties and absorption bands resonant with the emission wavelength of commercially available high power laser diodes make some Yb-doped materials such as Yb:YAG ideal candidates for high average power operation. Combined with specially engineered laser architectures that favor efficient heat dissipation, CPAs based on Yb-doped materials (from here on Yb-CPA) have enabled the generation of few-ps and sub-ps pulses with average powers exceeding 1 kW. At high repetition rates (tens of kHz to several MHz) the coherent combination of high power fiber lasers [59–61], the development of Yb:YAG thin-disk amplifiers [62–65] and the development of Innoslab amplifiers [66] have all led to the generation of sub-ps, mJ-level pulses at 1030 nm with average powers reaching the kW-level. Exploiting the enhanced thermo-mechanical properties and emission cross section of Yb:YAG at cryogenic temperatures, it has also been possible to develop an Yb-CPA delivering few-ps pulses with 1.1 J of energy at 1 kHz (1.1 kW average power) [67].

There are two ways in which these powerful sources can be implemented in attosecond science experiments: as pump lasers for OPCPAs or by significantly shortening the pulse duration through a nonlinear process. Yb-CPAs have been extensively employed as pump lasers for OPCPAs delivering CEP-stable few-cycle pulses at high average power and high repetition rate (see section 2.2). Most recently and thanks to the latest advances in nonlinear pulse compression these CPAs are being incorporated as the driver lasers in attosecond science experiments. In the next subsections we offer an overview of some of the relevant work published in the literature connected to both approaches. For a general overview on the latest advances in nonlinear pulse compression we refer the reader to a recent review article by Nagy *et al* [68].

2.1. Post-compression of high power CPAs

Nonlinear pulse compression relies on a spectral broadening process due to a third-order interaction of the laser electric field with the material in which the pulse is propagating. If the pulse intensity is sufficiently high, the polarization of the material, assuming a non-resonant interaction, contains a non-negligible term proportional to the third power of the electric field amplitude. This nonlinear term in the polarization locally changes the index of refraction (n) with a term proportional to the pulse intensity envelope (I), as shown in equation (2).

$$n = n_o + n_2 \times I(x, y, t). \tag{2}$$

Here, x, y are the spatial coordinates perpendicular to the propagation direction, t is time, and n_o and n_2 are the linear and nonlinear index of refraction, respectively. This nonlinear interaction, known as the optical Kerr-effect, induces a space- and time-dependent term in the index of refraction and leads to the well-known effects of self-phase modulation (SPM) and self-focusing [69]. SPM is responsible for spectral broadening and induces a positive chirp that is approximately linear. Therefore, compensation of the group-delay dispersion (GDD) utilizing dispersive mirrors leads to pulse durations much shorter than the original pulse. Note that due to the spatial dependence in equation (2), the spectral broadening and hence pulse shape, are not independent of the position across the beam any more, leading to space-time couplings.

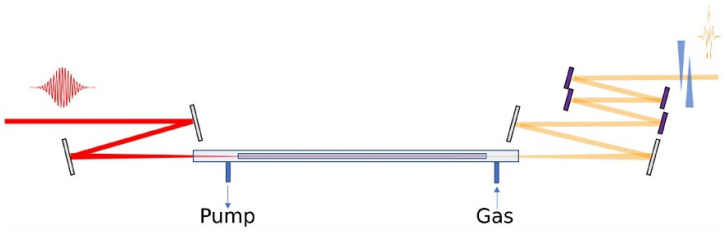

Figure 1. Sketch illustrating a hollow-core fiber compression setup with a pressure gradient configuration. The input pulses are focused into the fiber. At the output of the fiber the output beam is collimated and the pulses are compressed utilizing chirped mirrors.

The most widely applied technique for laser pulse post-compression is broadening of the pulse spectrum in a gas-filled hollow-core-fiber (HCF) followed by dispersion compensation with chirped mirrors [46]. This technique has become standard for the post-compression of few-mJ, few-kHz, sub-50 fs pulses from Ti:Sapphire CPAs and has led to the generation of sub-4 fs, multi- mJ pulses [70, 71] at 800 nm. A sketch of a typical setup is shown in figure 1. The input beam is focused at the input of the hollow fiber. In the case shown in figure 1 the HCF is operated under a pressure gradient configuration that minimizes ionization at the input [72]. After propagation through the hollow fiber and nonlinear interaction with the gas, the output beam is recollimated and the pulse is compressed utilizing chirped mirrors in combination with thin glass wedges for dispersion fine-tuning. The confinement of the laser pulse in the capillary allows keeping a high intensity over long distances ($>$1 m). This is necessary to accumulate a sufficiently high nonlinear phase and achieve substantial pulse broadening under a relatively weak nonlinear interaction of the intense pulses with the gas. In turn, this weak interaction makes the effect of self-focusing almost negligible, so that the spatial characteristics of the optical field are determined by waveguide propagation. In such a setup, the waveguiding effect of the HCF ensures a homogenenous spatio-temporal distribution of the output field [73].

A few years ago, post-compression in HCFs was extended to the post-compression of high average power, high repetition rate fiber-based Yb-CPAs. Sub-2 cycle pulses at a central wavelength of 1030 nm were produced at an impressive average power of 216 W with a repetition rate of 1.27 MHz (170 μJ pulse energy) after two consecutive HCF compression stages [58]. These results were further extended to compress much higher energy pulses in a single compression stage. Utilizing a 6 m long stretched flexible HCF, 300 fs pulses with 580 W of average power at 100 kHz (5.8 mJ pulse energy) were compressed down to 10 fs with an average output power of 318 W [74]. In both these experiments, the few-cycle pulses were not CEP-stable. However, by modifying the front-end of the CPA utilizing a commercially available carrier-envelope offset (CEO) frequency stabilized oscillator, CEP-stability with a residual noise of 330 mrad has been demonstrated for a double compression stage system delivering 100 μJ, 7.6 fs pulses at a repetition rate of 100 kHz [75].

It is worth mentioning that a fiber-based CPA in combination with nonlinear compression in HCFs has been presented as the method of choice at the extreme light infrastracture (ELI) facility for providing CEP-stable, few-cycle pulses with high average power and high repetition rate for experiments in attosecond science [76, 77]. Recently, one of these systems at ELI, featuring one compression stage, was utilized to generate APTs and perform pump-probe experiments [78–80].

Another nonlinear compression technique that has become widespread over the last few years is multi-plate supercontinuum generation (MPSC) [81]. The experimental implementation of MPSC is very simple and the system is impervious to pointing instability. The laser pulses to be compressed are focused to an intensity of approximately 1–10 TW cm^{-2}. At the position of the beam waist a very thin (typically $\ll$1 mm) glass plate is placed in order to broaden the bandwidth due to the nonlinear interaction of the laser pulses with the material. The thickness of the plate is such that, although self-focusing occurs, the position of the nonlinear focus is located outside of the plate. In other words, the pulse exits the glass plates before traversing the nonlinear focus. Outside of the glass plate self-focusing is much weaker and nonlinear focusing does not lead to ionization and plasma formation. However, there is a second beam waist in air, typically a few cm after the position of the first plate. Behind this position, a second thin plate is placed for further bandwidth enhancement. The procedure can be repeated several times. Figure 2 illustrates the idea.

Although this technique has been mostly used to compress sub-50 fs, sub-mJ pulses to the single cycle limit [83–85], direct compression of longer pulses from Yb-CPAs has been demonstrated. For example, Lu *et al* used a two stage setup to compress 170 fs, pulses from a Yb:KGW CPA operating at 100 kHz down to 3.21 fs, albeit at a relatively modest input average power of 6 W [86]. Meanwhile, Beetar *et al* utilized a

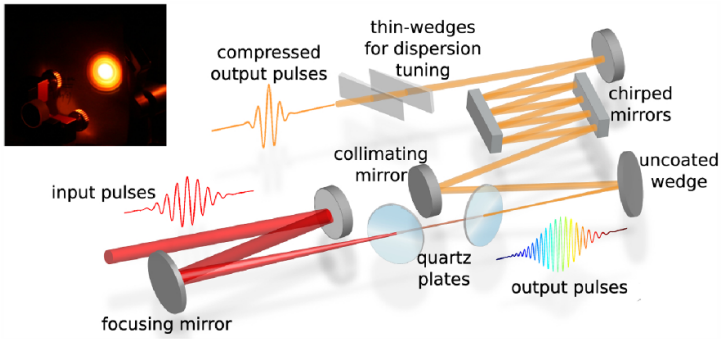

Figure 2. Illustration representing a multi-plate continuum generation setup. Reprinted with permission from [82] © The Optical Society.

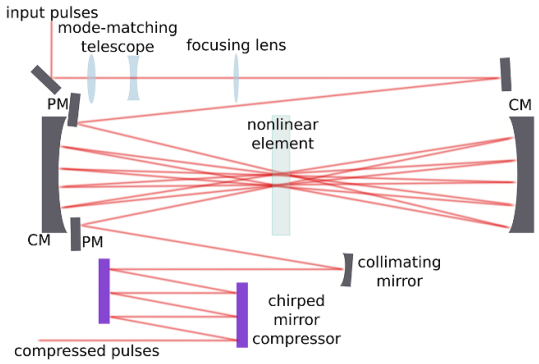

Figure 3. Sketch of a typical multi-pass cell compression setup where the nonlinear propagation takes place in a glass window (nonlinear element). The input beam is re-sized in a telescope and focused into the cell in order to match the mode of the cavity formed by the mirrors of the cell (CM). Two small plane mirrors (PM) are used to couple the beam into and out of the cavity. After spectral broadening the beam is collimated and the pulses are compressed by dispersion compensation with chirped mirrors.

similar scheme to compress 280 fs pulses with 20 W average power and 50 kHz repetition rate from a Yb:KGW CPA down to 18 fs [87].

A technique that can be considered as an extension of MPSC has been adopted by many groups worldwide to compress relatively long pulses. It consists of coupling the laser beam into a Herriot-type delay line or cell in which a piece of optical glass is placed at the location of the beam waist. Propagation through the glass is responsible for spectral broadening of the input pulses via SPM, in very much the same way as in MPSC [88]. The nonlinear interaction is tailored so that the nonlinear phase accumulation upon each pass through the material is small. However, the total accumulated nonlinear phase can be controlled by the number of passes through the cell. In this way, the technique allows for nonlinear propagation in a material over extremely long effective distances. In addition, propagation of the beam in the cavity effectively homogenizes the spatio-temporal distribution [89]. A variation of the technique consists of inserting the Herriot-cell in a chamber filled with a noble gas, where the nonlinear interaction is controlled by the type of gas and the pressure of the gas in the chamber. Figure 3 illustrates a typical multi-pass cell (MPC) compression setup. The technique has been successfully implemented to compress a variety of systems [90–95], but predominantly pulses at high power and high repetition rate from Yb-CPA systems. Some notable examples in the literature feature the compression of 1.1 mJ, 590 fs pulses at 500 kHz (600 W) from an Yb:YAG Innoslab-based CPA down to 30 fs and 1.06 mJ (530 W) in a single compression stage [96], compression of 1 mJ, 200 fs pulses at 1 MHz (1 kW) from an Yb-fiber CPA system down to 30 fs in a single compression stage [97], and the compression of 18 mJ, 1.3 ps pulses at 5 kHz from an Yb:YAG CPA based on thin-disk technology to 41 fs [98]. Recently, spectral broadening of 112 mJ, 1.2 ps pulses with a first-order helical Laguerre–Gaussian mode has been demonstrated, with a broadened spectrum supporting 37 fs pulses [99].

MPC compression is extremely well suited for the compression of relatively narrowband pulses with durations of hundreds of fs to a few ps, down to sub-50 fs pulse durations (for 1030 nm pulses), still well in the multi-cycle regime. Since MPC compression relies on a very weak nonlinear interaction per pass through the cell and a high number of passes, high reflectivity mirrors are essential. Approaching the few-cycle regime

then becomes challenging because the mirrors should have high reflectivity and low GDD over a very broad bandwidth, while at the same time having a high damage threshold. This regime of compression was studied with a two-stage MPC compression scheme. Balla *et al* demonstrated the compression of 1.2 ps, 2 mJ pulses at 100 kHz in bursts of 10 Hz from an Innoslab system, down to 13 fs in a cascaded setup implementing two consecutive MPC compression stages [100]. Furthermore, Müller *et al* recently demonstrated the compression of 200 fs, 1 mJ pulses at 500 kHz from a Yb-fiber-CPA down to 6.9 fs with 78% efficiency (excluding the dispersion compensation stage) in another two-stage MPC [101]. In order to handle the broad bandwidth and extreme average powers, the second MPC unit contained an array of dielectrically-enhanced silver-coated silicon mirrors that were actively cooled with water. Utilizing the same configuration, this group has recently reported the generation of CEP-stable 5.8 fs pulses with 107 W of average power at a repetition rate of 100 kHz [102]. Finally, MPC compression has been proposed and studied numerically for the compression of pulses from Ti:Sapphire systems with complex polarization states and Laguerre–Gaussian spatial modes [103, 104]. On top of that, very recently Rueda *et al* demonstrated the compression of sub-50 fs, 290 μJ pulses from a Ti:Sapphire CPA to 8 fs in a compact, gas-filled MPC [105]. These results are interesting in the context of extending MPC for the post-compression of high average power, high repetition rate OPCPAs with pulse energies in the same range. Shortly after, Daniault *et al* demonstrated the compression of 30 fs, 1 mJ pulses from a Ti:Sapphire CPA down to 5.2 fs [106], extending implementation of MPC compression of Ti:Sapphire CPAs to the mJ energy range. A recent review about nonlinear pulse compression in MPCs can be found in [107].

Combinations of some of the aforementioned techniques are also being implemented to generate few-cycle pulses directly from Yb-CPA systems. For example, Lavenu *et al* combined compression in MPC and compression in a large diameter core capillary, to demonstrate the generation of 6.8 fs, 140 μJ pulses at 150 kHz repetition rate (21 W average power) from a commercial Yb-fiber CPA [108]. By replacing the front-end of the CPA by a system based on difference frequency generation (DFG), the same group demonstrated that the nonlinearly compressed pulses from the CPA can be CEP stabilized [109].

It is worth mentioning that, with the latest advances in high power thulium fiber CPAs with a central wavelength around 2 μm, many of the results at 1 μm are being extended to the mid-IR [110, 111]. In fact, Gebhardt *et al* have recently implemented nonlinear pulse self-compression and soft-X ray generation in a single antiresonant hollow-core fiber from a 2 μm fiber CPA at 100 kHz [112].

2.2. Optical parametric chirped pulse amplifiers

The first approach implemented to overcome the limitations in repetition rate and average power of Ti:Sapphire CPAs was to develop OPCPAs pumped by high power, high repetition rate Yb-CPAs. OPCPA is an extension of optical parametric amplification (OPA) [113] in which the pulses to be amplified (in this context called seed or signal pulses) are stretched in time to approximately match the pulse duration of the pump pulses, and after amplification the pulses are compressed, very much like the CPA scheme for laser amplification [114]. Parametric amplification corresponds to the family of second order frequency conversion processes. In parametric amplification energy from a pump wave is transferred to a signal wave during the instantaneous nonlinear process. A third wave (the idler) is generated during the process with a frequency that corresponds to the difference between the pump and signal frequency, thus conserving energy, as indicated in the virtual energy level diagram of figure 4(a). It is therefore a DFG process. The gain and the gain-bandwidth are determined by phase matching conditions. In other words, the maximum gain is achieved when the absolute value of the phase mismatch $|\Delta\vec{k}|$ is minimized, where

$$\Delta\vec{k} = \vec{k}_p - \vec{k}_s - \vec{k}_i \tag{3}$$

and $\vec{k}_p, \vec{k}_s, \vec{k}_i$ are the k-vectors of the pump, signal and idler respectively. For example, in the case of type-I phase matching, the index of refraction of the extraordinary polarized pump wave is tuned by adjusting the angle θ between the crystal axis and the pump k-vector to achieve phase matching for a particular pair of ordinary polarized signal-idler frequencies (see figure 4(c)). In the case that the pump and seed beams are arranged in a noncollinear geometry, with a monochromatic pump and a broadband seed, the phase mismatch can be minimized over a broad range (see figure 4(d)) and the gain bandwidth is substantially increased [115], in some cases providing an amplification bandwidth that supports few-cycle pulses. The maximum bandwidth is found for a noncollinear angle α such that the group velocities of the signal and idler pulses are matched in the direction of propagation of the signal. As illustrated schematically in figures 4(b) and (c), phase matching in this case results in the frequency components of the idler being emitted in different directions, giving rise to an angularly dispersed idler beam. Since there is ideally no absorption in the nonlinear medium where the process takes place, there is no heat dissipation and therefore

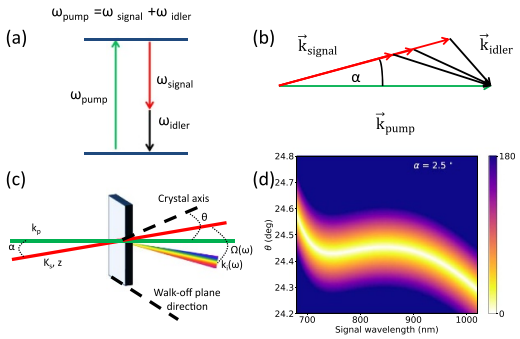

Figure 4. (a) Virtual energy levels diagram illustrating DFG. (b) k-vectors of pump, signal and idler waves illustrating phase matching in a noncollinear OPA. (c) Sketch illustrating the pump, signal and idler beams interacting in the nonlinear medium under type-I phase matching. (d) Phase mismatch map as a function of phase matching angle (θ) and signal wavelength for 515 nm pump and a 1 mm thick BBO crystal. The white regions indicate minimum phase mismatch.

OPAs are well suited for high average power operation. For a detailed description of OPAs and OPCPAs we refer the reader to some specialized textbooks and journal articles [116–119].

In addition to the ability to amplify pulses with broad bandwidth at high average powers, the CEP-stability of the amplified pulses is preserved during parametric amplification as long as the intensity of the pump pulses does not change substantially from pulse-to-pulse [119]. These characteristics make OPCPA a very attractive technique to amplify CEP-stable, few-cycle pulses to high energies at high repetition rates and, therefore at high average powers. It was already pointed out that Yb-CPAs, delivering mJ-level, few-ps and sub-ps pulses at high repetition rates ($\geqslant$100 kHz), offer excellent characteristics to pump high average power OPCPAs. Meanwhile, Ti:Sapphire oscillators are capable of delivering CEO-frequency-stable (i.e. constant CEP shift from pulse-to-pulse), few-cycle pulses ($<$6 fs at 800 nm) at low energy (few nJ). Direct amplification of low energy Ti:Sapphire oscillator pulses in a noncollinear OPCPA pumped by an Yb-CPA is therefore an ideal platform to extend the capabilities of Ti:Sapphire CPAs.

A few details concerning these type of OPCPAs are noteworthy. First, since the photon energy of the pump wave must be larger than the photon energy of the seed, the OPA stages must be pumped with a harmonic of the fundamental frequency of the Yb-CPA, typically the second harmonic. Second, for CEP-stable systems, the repetition rate of the pump has to be adjusted to a divisor of a fraction of the repetition rate of the seed. For example, if the CEO-frequency in the oscillator is locked to a $f_{rep}/4$, f_{rep} being the repetition rate of the oscillator, then the CEP slip from pulse-to-pulse in the oscillator pulse train is $\pi/2$. In that case, the repetition rate of the pump laser for the OPCPA must be a divisor of $f_{rep}/4$ in order to amplify only pulses that carry the same CEP. Third, for amplification around 800 nm, widely commercially available β-barium borate (BBO) crystals offer high nonlinearity and large amplification bandwidths for a noncollinear geometry under type-I phase matching. Finally, since parametric amplification requires spatial and temporal overlap of the interacting pulses in the nonlinear material, it is necessary that the seed and pump sources are synchronized. Electronic synchronization of the pump and seed laser sources [120] is one approach that has been implemented, mostly in systems in which the pump pulses have a duration of several tens of picoseconds [121, 122]. As an alternative to electronic synchronization, direct optical synchronization of both lasers sources has been achieved by seeding the pump laser with a fraction of the seed laser output that undergoes frequency shifting in a photonic crystal fiber, in order to match the gain-bandwidth of the pump laser amplifiers [123]. With the advent of commercially available ultra-broadband (octave-spanning) Ti:Sapphire oscillators, the frequency shifting stage can be eliminated and the complexity of the system reduces significantly. This approach has been implemented by several groups to generate CEP-stable, sub-10 fs pulses at 800 nm at high repetition rates ($\geqslant$100 kHz—few-MHz) at average powers ranging from a few W to more than 20 W [124–131]. This is moreover the architecture of choice for the OPCPA driving the high repetition rate attosecond pump-probe beamline at the Max-Born-Institute (MBI) [132–134], that will be introduced in the next section. Furthermore, with the same synchronization scheme, but combining OPA stages pumped by the second and third harmonics of an Yb-CPA respectively, Harth *et al* have demonstrated direct amplification of ultra-broadband pulses covering 1.5 octaves at 200 kHz, supporting sub-3 fs pulses [135].

Another way of achieving optical synchronization between the pump and seed pulses is to derive both pulses directly from the Yb-CPA. There are slightly different ways of implementing this concept but the basic idea is to produce the broadband seed pulses through coherent supercontinuum generation in bulk via

filamentation [56, 136]. A comprehensive review of supercontinuum generation can be found in [137]. In order to achieve CEP stability, either the Yb-oscillator driving the CPA can be phase-stabilized or the short-pulse front-end can be based on a combination of nonlinear frequency conversion processes involving supercontinuum generation and DFG [138, 139]. Fattahi *et al* have dubbed this OPCPA architecture driven solely by Yb-CPA systems as third-generation femtosecond technology [140]. Numerous examples exist in the literature of such systems operating around 800 nm and offering a high average power alternative to Ti:Sapphire CPAs. Most notably, the OPCPA system developed for experiments at the LCLS-II x-ray free-electron laser facility delivers sub-20 fs pulses at 100 kHz at an average power of 88 W [141].

Besides operation at 800 nm, the same architecture based on Yb-CPAs that was previously described, represents an ideal platform to generate ultrashort pulses with high average power and high repetition rates in the mid-IR. In this case, alternative nonlinear materials such as Potassium Titanyle Arsenate ($KTiOAsO_4$) or KTA, with transparency windows extending deep into the mid-IR, provide a route toward the operation of high power OPCPAs [142–149]. Moreover, Elu *et al* have implemented soliton self-compression of mid-IR OPCPA pulses in a gas-filled anti-resonant photonic crystal fiber to generate near single cycle pulses around 3 μm at 160 kHz with 9 W of average power [150]. In the context of attosecond science, moving to longer driving wavelengths is attractive to generate higher photon energies [151] due to the scaling of HHG with the wavelength of the driver [152]. For example, recently high harmonics in the water window have been demonstrated at a repetition rate of 100 kHz, driven by a 25 W OPCPA delivering few-cycle pulses at 2.2 μm [153]. Additionally, in experiments on laser-induced electron diffraction [154], long wavelength drivers allow reaching higher recollision energies and greatly simplify the analysis, since the electronic wavepacket returning to the parent ion can be better approximated by plane waves.

Power scaling of high repetition rate OPCPAs requires adequate thermal management. The extremely small absorption coefficients over the transparency windows of nonlinear crystals usually renders the heat dissipation negligible. However, when the pump power approaches the kW-level [141, 149], absorption of the pump and the long wavelength components of the idler in BBO [129, 155, 156] for example, or absorption of the pump in the anti-reflection coatings of the crystal [129], begin to affect the amplifier performance. Not only can the induced thermal gradients affect phase matching through local changes in the index of refraction, but this spatial dependence of the phase matching process can lead to complex spatio-temporal couplings in the amplified pulses. Moreover, in extreme cases thermally-induced mechanical stress can induce crystal damage. Riedel *et al* have compared the performance of different borate crystals for high power operation and have proposed heat management solutions for power scaling [155]. Meanwhile, Baudisch *et al* have analyzed the performance of MgO:PPLN, KTA and $KNbO_3$ for high power operation in the mid-IR [157]. It is worth noting that operation of a 88 W, 100 kHz OPCPA at 800 nm [141] did not require special thermal management since the relatively small thermal gradients in the crystal (2.0 K cm^{-1}) and the high thermal acceptance of BBO made thermally-induced phase mismatch negligible. Further increase in pulse energy (and consequently average power) beyond the results reported in [141] is limited by the available pulse energy of high repetition rate CPAs utilized as pump lasers. Therefore, an increase in OPCPA pulse energy is directly linked to further developments in high repetition rate, high average power picosecond CPAs. Additionally, an increase in pulse energy requires larger apperture crystals. High average power OPCPA systems operating at 800 nm based on BBO crystals have been demonstrated at pump pulse energies as high as 150 mJ [158] with a repetition rate of 1 kHz. At higher pulse energies, different nonlinear crystals with larger apertures such as KDP or LBO are required [159], or novel approaches such as double-chirp OPA can be implemented [160, 161].

2.3. High power, high repetition rate NIR-OPCPA at the MBI

The high-repetition rate Attosecond Laboratory at the MBI has been established with the aim of performing attosecond pump-probe experiments with coincidence detection of electrons and ions utilizing a ReMi. In order to reach the demanding requirements of coincidence detection in the context of attosecond experiments, a high power, high repetition rate OPCPA has been developed, based on the combination of an ultrabroad bandwidth Ti:Sapphire oscillator and an Yb-CPA. In this section this OPCPA and its characterization are described. In addition, two approaches for post-compression to the single-cycle limit are presented.

2.3.1. OPCPA

Figure 5 shows a block diagram representing all the main components of the OPCPA system. The corner stone of this complex system is the Ti:Sapphire oscillator. This commercial laser (Venteon Femtosecond Technologies, nowadays part of Laser Quantum GmbH) delivers sub-6 fs pulses at 800 nm at a repetition rate of 80 MHz with an average power of approximately 240 mW (pulse energy 3 nJ). Within the enclosure of the oscillator, a small fraction of the output is transmitted through a partial reflector and sent to an f-2f

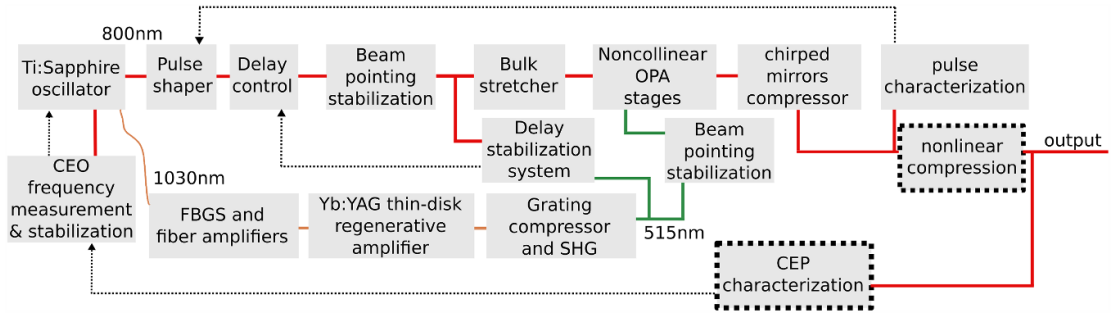

Figure 5. Block diagram representing the main components of the system. The solid red lines represent 800 nm (broadband) laser beams, the solid orange lines represent 1030 nm laser beams, and the solid green lines represent 515 nm laser beams. The curved, thin, orange line connecting the oscillator box and the fiber amplifier box represents an optical fiber guiding the seed pulses for the CPA at 1030 nm. The black dotted lines with arrow heads represent electronic signals in a feedback loop. The thick dotted lines around the nonlinear compression and CEP-characterization blocks indicate that the OPCPA can be operated without these additional features. See text for more details.

interferometer for measuring the CEO frequency. The bandwidth of the oscillator pulses covers a full octave. Therefore, there is no need for additional spectral broadening in the f-2f interferometer. The CEO frequency is stabilized to $1/4$ of the repetition rate using a commercial system (XPS800-E, Menlo Systems GmbH) that generates a signal driving an acousto-optic modulator that modulates the pump power. That means that the phase slip from pulse-to-pulse in the 80 MHz pulse train of the oscillator is $\pi/2$. A dichroic mirror with a transmissive window around 1030 nm, also located inside the oscillator's enclosure, separates the 800 nm seed for the OPA stages from the 1030 nm seed for the CPA. The 1030 nm pulses are coupled into a single-mode polarization maintaining optical fiber and sent to the Yb-CPA system. As explained in the previous section, this optical link achieves the synchronization of the two laser sources interacting in the OPA stages.

At the output of the oscillator the spectral phase of the 800 nm pulses from the oscillator is pre-shaped in a 4f-pulse-shaper based on a spatial light modulator (SLM) (MIIPS Box 640 P, Biophotonics Solutions Inc.). This step becomes relevant during pulse compression after amplification. At the output of the pulse-shaper, a spatial filter cleans up the spatial profile of the beam (not shown in figure 5). After losses in the pulse shaper, the spatial filter, and the delay stabilization system (see below), approximately 20 mW (pulse energy 250 pJ) reach the first OPA stage.

The pump laser for the OPCPA is a commercial Yb-CPA system from Trumpf Scientific Lasers GmbH. The CPA consists of a fiber Bragg grating stretcher (FBGS), three fiber-based pre-amplification stages, a main amplifier, a grating compressor and a second harmonic generation (SHG) stage, all shown in separate blocks in the diagram of figure 5. The 1030 nm pulses from the polarization maintaining fiber, with an average power of 0.4 mW (pulse energy 5 pJ) are amplified in a first fiber amplifier. Subsequently the pulses are stretched in time in the FBGS and amplified in a second fiber amplifier before the repetition rate is reduced to 2 MHz by means of a pulse-picker. A third fiber-based amplification stage brings the average power to 15 mW. The all-fiber system was developed by Laser Quantum GmbH and integrated into the CPA system by Trumpf Scientific Lasers GmbH. The pulses that were pre-amplified in the fiber-system seed the main amplifier, an Yb:YAG thin-disk regenerative amplifier operating at a repetition rate of 100 kHz. Then, the pulses are compressed in a reflective-grating stretcher. Inside the compressor, a two-point beam pointing stabilization system (beam position detected and corrected in two different positions along the propagation coordinate) corrects for drifts in the pointing of the output beam over long periods of time (not shown in figure 5). This Yb-CPA delivers up to 190 W of average power, 1 ps pulses at a repetition rate of 100 kHz (pulse energy 1.9 mJ). Finally, the pulses are frequency doubled in an LBO crystal in order to produce pulses at 515 nm to pump the OPCPA. The OPCPA pump pulses have an average power of 120 W (pulse energy 1.2 mJ) and a pulse duration of 900 fs. A detailed description of the Yb-CPA can be found in [130].

The 515 nm pump beam is split using a set of $\lambda/2$ waveplates and polarizers. 12 W are sent to the first OPA stage, 5 W are sent to an auxiliary OPA stage for controlling the pump-seed delay, and the rest is sent to the second OPA stage. In the second stage pump arm, an additional $\lambda/2$ waveplate-polarizer set controls the pump power into the second OPA stage. The maximum pump power available for the second stage is 96 W. The pump beam in all three OPA stages is extraordinary polarized, with the polarization vector parallel to the plane of the optical table. In both amplification stages, the pump beam pointing into the crystal is detected with a quadrant position photodiode (PDQ80A, Thorlabs Inc.) and stabilized utilizing one mirror mount with piezoelectric actuators. In both cases, a leak from a steering mirror is used for detection, introducing no

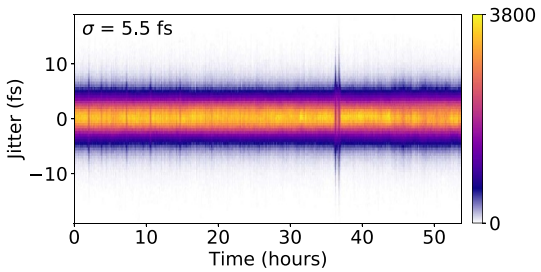

Figure 6. Two-dimensional histrogram illustrating the measured residual jitter in the pump-seed delay over more than 50 h of uninterrupted operation.

additional losses. Although the block in the diagram of figure 5 indicates a single beam pointing stabilization system, it should be interpreted as two independent systems, one for each amplification stage.

As described previously, the pump and seed pulses in the OPA stages are synchronized because they share the same oscillator. However, the optical path of the pump pulses from the point where the 800 and 1030 nm beams are split (in the oscillator) to the point where they meet in the first OPA stage, is significantly longer than the optical path of the seed pulses. The pump pulses undergo several tens of meters of propagation in optical fibers in the stretcher and pre-amplification stages, and more than 100 m of propagation in the regenerative amplifier. This implies that in order to satisfy time-overlap of the seed and pump pulses in the OPA stages, the pump pulse overlaps with a later pulse from the oscillator, and not the same pulse from which it was split. More important, small changes in temperature, vibrations affecting the optical components and air turbulences introduce perturbations to the arrival time of the pulses to the OPA stages, affecting the time overlap and hence the amplification process. Therefore, for stable operation of the OPCPA it is necessary to stabilize the delay between pump and seed pulses. Several methods have been proposed in the literature [162–165]. We implemented a variation of the method proposed in [165] that incorporates all-digital data processing. The delay stabilization block in figure 5 contains an auxiliary noncollinear OPA stage tailored to maximize the sensitivity of the amplified output spectrum to changes in the delay between the pump and seed pulses. 3% of the seed power is split from the main beam utilizing a partial reflector and sent to the auxiliary stage. The seed pulse for the auxiliary stage is then stretched in a 5 cm thick block of SF-11 to a duration significantly longer than the pump pulse duration. In that way, only the small fraction of the chirped pulse that is overlapped in time with the pump pulse gets amplified. Thus, the amplified bandwidth is much narrower than the seed bandwidth, and the central wavelength depends on the pump-seed delay. The choice of stretching factor presentes a dilemma. In order to cover a large delay range of the stabilization system, a large stretching factor is required. However, in turn the fractional wavelength change for a pump-seed delay change is anti-proportional to the stretching factor. In the setup described above, the central wavelength of the amplified signal spectrum shifts 0.03 nm fs^{-1}. The seed pulses in this auxiliary OPA stage are amplified in a 3 mm thick BBO crystal under type-I phase matching and the amplified spectrum is detected with a commercial spectrometer (Flame-S-VIS-NIR, Ocean Optics Inc.). A control software was developed in Python that compares the measured amplified spectrum to a reference spectrum and derives a feedback signal that is sent to the delay control unit. The time of arrival of the seed pulses to the OPA stages is controlled by two linear stages. A first linear stage with a piezoelectric actuator (PIHera P-622.1CD, Physik Instrumente GmbH) receives the feedback signal from the software and provides a fast correction to the pump-seed delay. The bandwidth of this feedback loop is approximately 110 Hz. However this stage has a limited travel range of 250 μm. The delay stabilization system software monitors the position of the piezoelectric actuator and controls an additional linear stage with a travel range of 48 mm (SuperAgilis, MKS/Newport Corporation). When the piezoelectric actuator approaches one of the two ends of its travel range, the additional linear stage is moved, so that the piezoelectric actuator goes back to the center of its range. With this system a residual pump-seed delay jitter below 6 fs has been achieved, over days of operation, ensuring stable performance of the OPCPA during experiments taking place over several days. Figure 6 shows a two-dimensional histogram illustrating the residual pump-seed delay jitter recorded by the control software over more than 50 h of uninterrupted operation. The control software allows recording the performance of the system during a pump-probe experiment, offering the chance to identify intervals during an experiment where the stability of the OPCPA underperforms.

In between the delay control and the amplification stages, the pointing of the seed beam is stabilized with a commercial two-point stabilization system (Aligna, TEM Messtechnik GmbH). Subsequently the pulses are stretched in 5 mm of fused silica. At the input of the first OPA stage, the seed pulses have an approximate

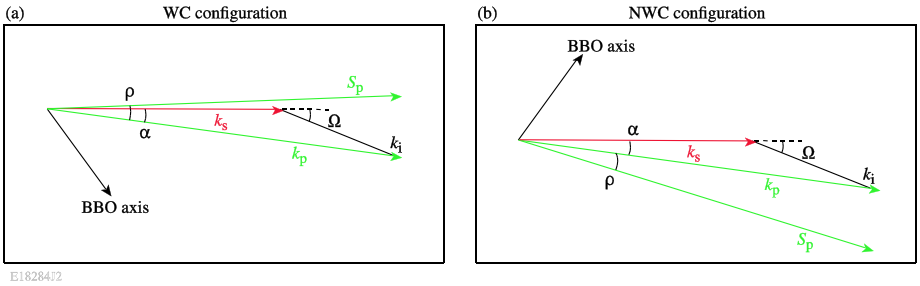

Figure 7. Phase matching geometries in noncollinear OPA in BBO under type-I phase matching. k represents the k-vector of pump (p), signal (s) and idler (i) respectively. S_p represents the Poynting vector of the pump. α, Ω, ρ are the noncollinear angle, the frequency-dependent angle between the idler and the signal k-vectors, and the walk-off angle (see text), respectively. (a) WC: the Poynting vector moves toward the signal. NWC: the Poynting vector moves away from the signal. Reprinted with permission from [166] © The Optical Society.

duration of 300 fs. The seed beam is vertically polarized and the polarization direction is perpendicular to the optical axis of the birefringent BBO crystal (ordinary wave). The seed pulses are amplified in two consecutive noncollinear OPA stages under type-I phase matching (i.e. the signal and idler are ordinary waves, the pump is an extraordinary wave). The noncollinear angle α inside the crystals is 2.5° and both amplification stages are set in the walk-off compensation geometry (WC) [166]. The implications of this geometrical configuration will be discussed later. The pulses are amplified to 12 μJ (1.2 W) in the first stage in a 2.5 mm thick BBO crystal, which is pumped at an intensity of 100 GW cm^{-2}. Upon beam collimation, the pulses are further amplified to 240 μJ (24 W) in a 3 mm thick BBO crystal pumped at an intensity of 50 GW cm^{-2}. The BBO crystal of the second OPA stage is located inside a box flushed at all times with dry nitrogen, with small openings for the input and output beams. The temperature of the crystal is controlled with a Peltier element and kept at 40 °C.

The amplification stages were designed following the guidelines presented in [167] in order to reach a compromise between high extraction efficiency in the amplifier and weak spatio-temporal couplings. The modest conversion efficiency in the first stage was designed to minimize spatio-temporal distortions due to saturation effects. The possible phase matching geometries are illustrated in figure 7, taken from [166]. Since BBO is a negative uniaxial crystal, the Poynting vector of the extraordinary wave (the pump in this case), subtends an angle ρ with the k-vector. After propagation in the material, the beam is displaced. In the WC shown in figure 7(a), the pump beam is displaced toward the signal beam, partially compensating the walk-off between the beams due to the noncollinear geometry. Meanwhile, in the non-walk-off compensation geometry (NWC) illustrated in figure 7(b), also known as tangential phase matching, the pump beam walks away from the signal beam, increasing the walk-off effect due to the noncollinear geometry.

In the WC geometry, phase matching for SHG of seed and idler is satisfied, and therefore there is a fraction of the output power (as much as 10%) that is lost to these parasitic effects. In addition, the parasitic sum-frequency processes modulate the amplified spectrum [166]. For multi-mJ pump beams, where the size of the beam is much larger than the walk-off between the beams in the crystal, the NWC geometry is usually preferred. However, at lower energies, when the sizes of the beams become comparable to the walk-off between the beams, the NWC induces degradation of the beam quality in the near field and strong spatio-temporal distortions, which in turn lead to degradation of the achievable peak intensity [166, 167]. This is illustrated in figure 8, reproduced from [167]. Figure 8 analyzes the evolution of the conversion efficiency with crystal length for amplification of 800 nm Gaussian pulses (600 fs FWHM) with a Gaussian spatial profile, and pump pulses at 515 nm with a duration of 1 ps FWHM. In the figures, the solid red squares (blue triangles) correspond to results of amplification efficiencies for a Gaussian (Super-Gaussian) pump beam profile with a beam waist of 0.5 mm and a peak intensity of 100 GW cm^{-2}. Meanwhile, the empty red squares (blue triangles) quantify the degradation of the peak intensity as the conversion efficiency increases. In this case the definition of the Strehl ratio, denoting the ratio of peak image intensities between the images from a real optical system illuminated by a point source and an aberration-free system, has been adapted to quantify the degradation of peak intensity due to spatio-temporal aberrations in broadband laser pulses. For details on the calculations we refer the reader to the original publication [167]. Figures 8(a) and (b) show a comparison of the conversion efficiency and degradation of the peak intensity for the WC and NWC geometries respectively. The numerical results show that at this pump energy level, the WC geometry not only provides higher conversion efficiencies, but also is less prone to peak intensity degradation due to space-time couplings.

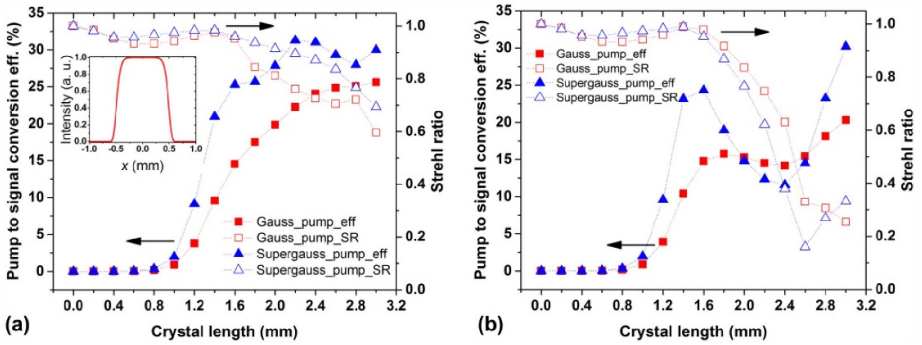

Figure 8. Conversion efficiency as a function of crystal length for (a) WC geometry and (b) NWC geometry. In both cases results with Gaussian (solid red squares) and Super-Gaussian (solid blue triangles) beam profiles are shown. The axes on the right show the evolution of the Strehl ratio (empty squares and triangles), defined here as the ratio of the peak intensity of the amplified pulse, compared to a reference pulse in which all spatio-temporal distortions have been removed (see details in [167]). The pump pulse energy in all cases is in the order of 0.5 mJ. Reprinted with permission from [167] © The Optical Society.

For the experimental system under consideration then, the WC geometry helps minimizing space-time couplings, in particular in the first stage where the beam walk-off between pump and seed due to the noncollinear geometry is comparable to the diameters of the interacting beams. In the second stage, the losses to parasitic SHG of the idler reduce the back-conversion effect, thus increasing the energy extraction efficiency of the seed [167]. In total, less than 5% of the output power correspond to parasitic second harmonic of the amplified signal. The parasitic second harmonic is removed in the compressor, since the compression mirrors have low reflectivity around 400 nm.

After amplification the pulses are partially compressed utilizing a set of chirped mirrors (Laser Quantum DCM11) and a pair of thin fused silica wedges for dispersion fine tuning, in order to minimize the GDD. Note that for optimization of the OPA stages and this first compression step, a flat phase is introduced in the SLM of the pulse shaper. Then, the pulses are characterized along one spatial dimension across the beam utilizing the SEA-F-SPIDER technique [73] with a multiple-shearing algorithm [168]. From the spatially integrated pulse reconstruction, the spectral phase is used as feedback for the pulse shaper; i.e. minus the measured phase is loaded as a mask in the SLM. This procedure allows compensating for high-order dispersion terms in the spectral phase and improves the pulse compression significantly.

Figure 9 shows the characterization of the pulses along two perpendicular directions across the beam profile, after optimization using the pulse shaper. A spatially-resolved analysis of the amplified pulse is essential to characterize and minimize space-time couplings, which are ubiquitous in noncollinear OPAs. [167, 169, 170]. Figure 9(a) shows the spectrum as a function of the spatial coordinate parallel to the direction of beam walk-off in the OPA stages (from here on, walk-off direction), while figure 9(b) shows the corresponding results along the direction perpendicular to the walk-off direction (from here on, perpendicular direction). As mentioned before, the design of the OPA stages followed guidelines intended to minimize space-time couplings. Nevertheless, small deviations from the designed parameters due to alignment imperfections for example, may lead to a small amount of residual angular dispersion of the amplified beam along the walk-off direction (see figure 4) [169]. Spatio-temporal characterization of the amplified pulses is essential to minimize the degradation of the peak power through spatio-temporal distortions [133, 167].

Figure 9(a) shows a clear dependence of the spectral shape of the amplified pulses on the position along the walk-off direction, specially for short wavelengths below 750 nm. Meanwhile, along the perpendicular direction (figure 9(b)) the dependence is almost negligible. Since the SEA-F-SPIDER characterizes the pulses at the focal plane of a focusing mirror, where a doubling crystal is placed for the necessary frequency conversion step to take place, residual spatial chirp in the spatio-spectral distribution is a sign of angular dispersion in the amplified beam leaving the OPA stages. Figure 9(a) shows that angular dispersion arising from misalignment of the noncollinear angle has been minimized in this case. Figures 9(c) and (d) show spatially integrated spectra (in red) along both directions. The integrated spectra along the two directions are very similar and lead in both cases to a Fourier-transform limited pulse duration of 5.6 fs. In both figures, the results of ten consecutive measurements taken are shown. In addition, the spatial average of the retrieved spectral phases corresponding to all individual measurements are shown (dotted green lines). The retrieved spectral phases are rather flat over the entire spectrum thanks to the compensation mask introduced in the pulse shaper. Figures 9(e) and (f) show the corresponding reconstructed pulse envelopes as a function of position along the walk-off and perpendicular directions respectively. Again, the dependence on the position

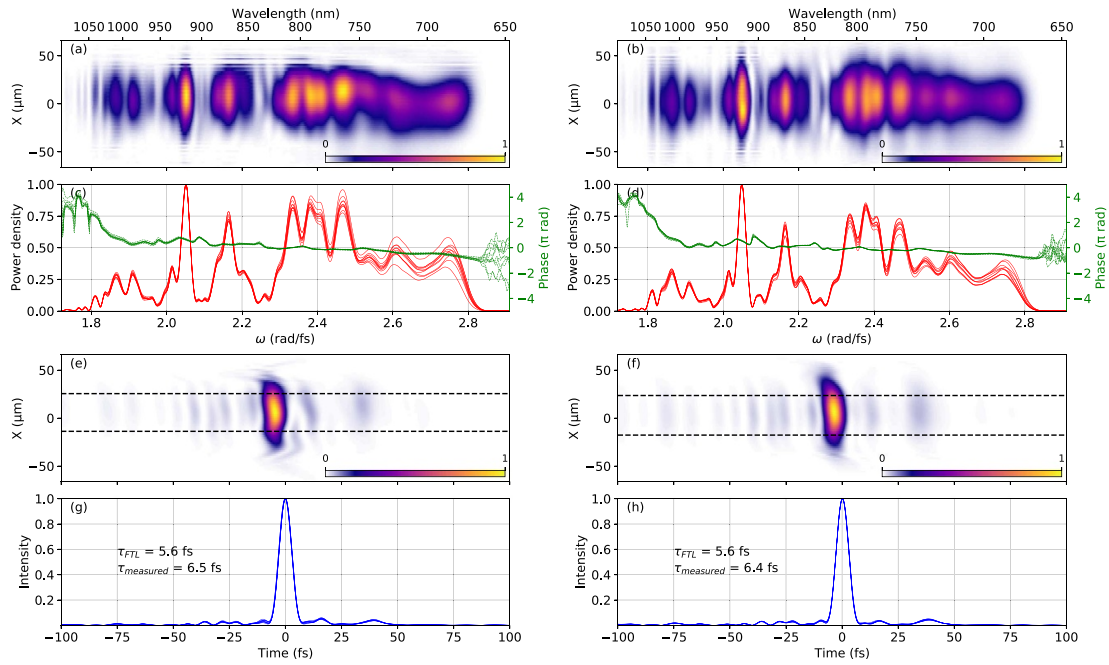

Figure 9. SEA-F-SPIDER characterization of the amplified pulses. (a) Spectrum as a function of the position along a line across the amplified beam parallel to the walk-off plane in the OPA stages. (b) Same measurement along the perpendicular direction. (c) and (d) Retrieved spectra and spectral phases after integration over the spatial coordinate in (a) and (b) respectively (ten consecutive measurements shown). (c) Absolute value squared of the reconstructed pulse envelope as a function of position for the walk-off (e) and perpendicular (f) directions. Retrieved pulse envelopes (ten measurements shown) for the walk-off (g) and perpendicular (h) directions after integration over the spatial coordinate within the dashed lines indicated in (e) and (f) respectively, which mark the point where the intensity in the spatial distribution falls to 1/2 of the maximum.

along the beam is modest. The spatially integrated pulse durations are shown in figures 9(g) and (h) for the walk-off and perpendicular directions. In both cases the integrated pulse duration is below 7 fs FWHM. The flat spectral phase over almost the full spectrum leads to clean temporal shapes without strong satellites; i.e. pre- and post- pulses have an intensity that is less than 3% of the main pulse intensity.

After losses in the compression stage and beam steering optics, the maximum output power is 19 W, corresponding to a pulse energy of 190 μJ. The pulse-to-pulse energy stability measured over several minutes is characterized by a standard deviation of 1.5% of the pulse energy, while the output power stability over several hours of operation is characterized by a standard deviation of 1% of the total power. The delay-stabilization system and the various beam pointing stabilization stages are essential for achieving a stable operation of the OPCPA.

2.3.2. Nonlinear pulse compression

With the pulse energy and pulse duration described in the previous subsection, the system satisfies the requirements for implementation of the polarization gating technique for the generation of IAPs [39]. However, the 2.5 optical cycles duration of the pulses would significantly limit the HHG efficiency with a polarization modulated in time. In order to bring the pulse duration closer to the single-cycle limit, enabling also other gating methods, two approaches for nonlinear pulse post-compression have been evaluated: MPSC generation and gas-filled hollow core fiber compression. In what follows, the main results are summarized.

In the case of MPSC, compressed pulses from the OPCPA at a reduced power of 14 W (the main limitation being the available space in the laboratory) were focused in air to an approximate intensity of 30 TW cm^{-2}. The spectral broadening took place in two 50 μm thick plates of quartz in a Brewster angle configuration, although SPM in air produced a non-negligible contribution as well. After recollimation and compression utilizing chirped mirrors (PC70, Ultrafast Innovations GmbH) and a pair of thin fused silica wedges, the output power was 68% of the input power. This throughput takes into account spatial filtering of outer rings in the beam that are a result of conical emission during the nonlinear propagation [81]. Once again, the SEA-F-SPIDER technique was utilized for pulse characterization along one spatial coordinate across the beam. Figure 10 show the characterization of the pulse along the walk-off and perpendicular directions.

Figures 10(a)–(d) show the spatio-spectral distributions and corresponding spatially integrated spectra covering more than one full octave and supporting compression to 1.3 optical cycles. Dispersion

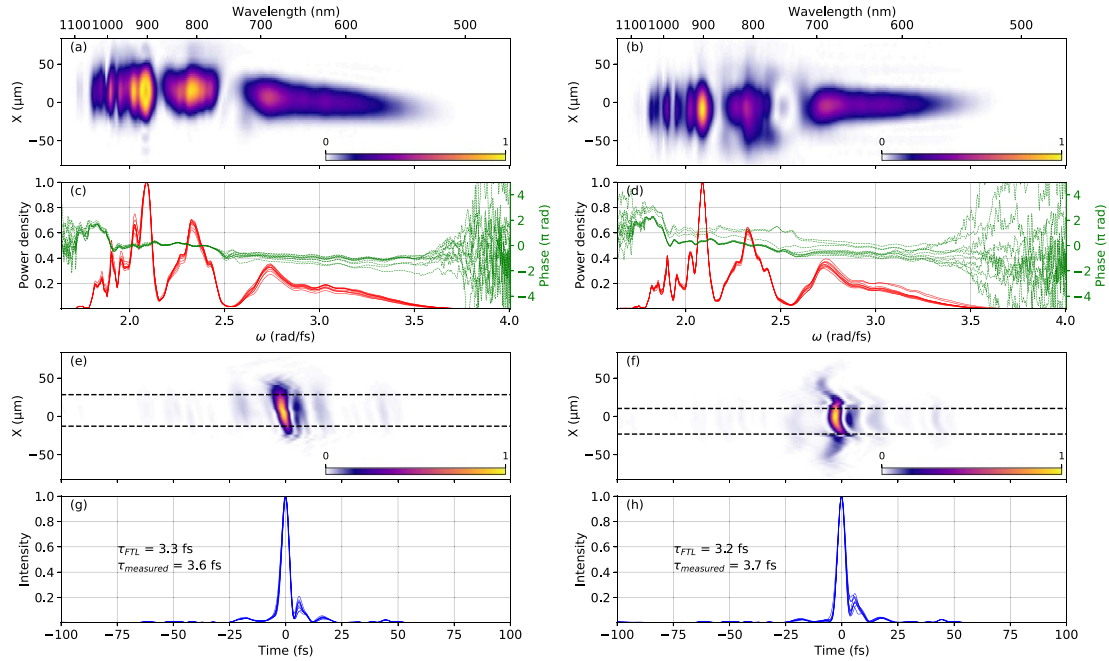

Figure 10. SEA-F-SPIDER characterization of the pulses compressed with the MPSC technique. (a) Spectrum as a function of the position along a line across the beam, parallel to the walk-off plane in the OPA stages. (b) Same measurement along the perpendicular direction. (c) and (d) Retrieved spectra and spectral phases after integration over the spatial coordinate in (a) and (b) respectively (ten consecutive measurements shown). (c) Absolute value squared of the reconstructed pulse envelope as a function of position for the walk-off (e) and perpendicular (f) directions. Retrieved pulse envelopes (ten measurements shown) for the walk-off (g) and perpendicular (h) directions after integration over the spatial coordinate within the dashed lines indicated in (e) and (f) respectively, which mark the point where the intensity in the spatial distribution falls to 1/2 of the maximum. Adapted with permission from [82] © The Optical Society.

compensation allowed compressing the pulses to 3.6 fs across the horizontal direction and 3.7 fs across the vertical direction, corresponding to approximately 1.5 and 1.6 optical cycles respectively. The spatio-spectral (figures 10(a) and (b)) and spatio-temporal (figures 10(e) and (f)) distributions show spatio-spectral couplings characterized by a frequency-dependent beam size and position dependent pulse shape. On top of that, in the horizontal direction, a clear spatial-chirp is observed at high frequencies, which originates from the Brewster angle configuration. In the horizontal direction the input spectrum is angularly dispersed inside the quartz plates, and the angular dispersion is corrected when the beam emerges in air. However, the new frequency components generated inside the plates are generated parallel to the input beam and they suffer from angular dispersion when they leave the plates. This observation is supported by a measurement of the normalized spatial chirp ($\rho_{x\omega}$) defined by Gabolde *et al* [171]:

$$\rho_{x\omega} = \frac{\int\int x\omega I(x,\omega)dxd\omega}{\sqrt{\int\int\int I(x,\omega)\omega^2 dxd\omega \int\int I(x,\omega)x^2 dxd\omega}}, \tag{4}$$

where $I(x,\omega)$ is the spatio-spectral distribution. For the data of figures 10(a) and (b) the average over ten measurements of $\rho_{x\omega}$ is -0.04 and 0.003 respectively, clearly showing an order of magnitude higher spatial chirp along the walk-off direction in the far field (i.e. angular dispersion in the near field). Repeating the experiment with the plates at normal incidence, the normalized spatial chirp along the walk-off direction was reduced to -0.002 and 0.009 for the horizontal and vertical directions respectively. Beside the spatio-temporal characterization of the pulses, Lu *et al* also presented frequency-resolved measurements of the beam in the far- and near-field, illustrating the non-negligible space-time couplings [82]. Nevertheless, this simple setup proved effective for compressing the OPCPA pulses to 1.5 optical cycles.

In the second nonlinear compression approach, the compressed pulses from the OPCPA were focused into a 1 m long HCF with a core diameter of 340 μm operated in a pressure gradient configuration. Filling the HCF with 3.0 bars of Ne, the spectrum was broadened to more than one octave and after dispersion compensation with chirped mirrors (PC70, Ultrafast Innovations GmbH) and a pair of thin fused silica wedges, the pulse duration was reduced to approximately 1.5 optical cycles. Compared to the previous case, for the same input power of 14 W into the HCF, the output power of the compressed pulses reached 7 W

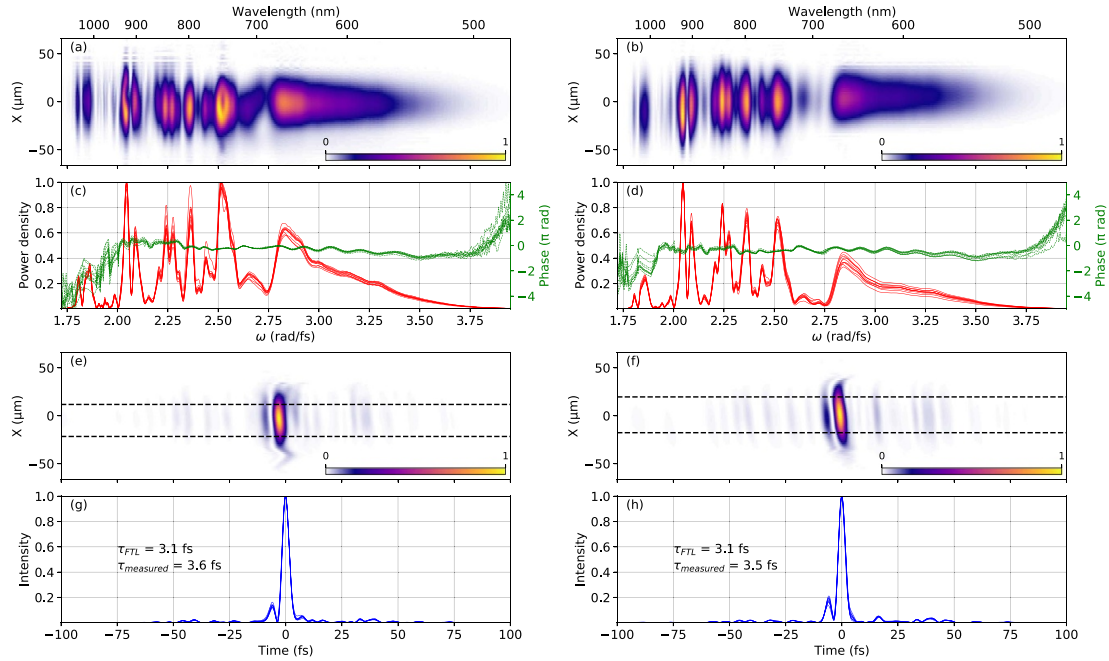

Figure 11. SEA-F-SPIDER characterization of the pulses compressed with the HCF technique. (a) Spectrum as a function of the position along a line across the beam, parallel to the walk-off plane in the OPA stages. (b) Same measurement along the perpendicular direction. (c) and (d) Retrieved spectra and spectral phases after integration over the spatial coordinate in (a) and (b) respectively (Ten consecutive measurements shown). (c) Absolute value squared of the reconstructed pulse envelope as a function of position for the walk-off (e) and perpendicular (f) directions. Retrieved pulse envelopes (Ten measurements shown) for the walk-off (g) and perpendicular (h) directions after integration over the spatial coordinate within the dashed lines indicated in (e) and (f) respectively, which mark the point where the intensity in the spatial distribution falls to 1/2 of the maximum.

(50% efficiency). Because of the wave guiding effect of the HCF, a radially symmetric spatio-temporal distribution is to be expected. Figure 11 shows the pulse characterization along the walk-off and perpendicular planes. Note that these measurements and the measurements in figure 9 were taken on the same day, so a direct comparison can be made.

The spatio-spectral distribution of figures 11(a) and (b) shows a weak dependence of the spectrum with position, especially at short wavelengths below 700 nm. Essentially, the broadened part of the spectra in the VIS, in both cases, presents an almost negligible dependence on the position. Meanwhile, the NIR part of the spectra in figures 11(a) and (b) resembles the original OPCPA spectra shown in figures 9(a) and (b). In particular, the small kink in the OPCPA spatio-spectral distribution along the walk-off direction, between 700 and 750 nm, appears to have survived during nonlinear propagation in the HCF.

The spatially-integrated spectra of figures 11(c) and (d) (red lines) cover well over one full octave and the retrieved spectral phases after compression (green dotted lines) remain relatively flat over the full spectrum. Once again, the results of ten consecutive measurements are shown. The spatio-temporal profiles of figures 11(e) and (f) show minimal distortions. The spatially integrated pulse shapes are shown in figures 11(g) and (h). The spatially integrated pulse durations (average over ten measurements) were 3.6 and 3.5 fs FWHM (below 1.5 optical cycles) for the measurements along the walk-off and perpendicular directions respectively, while the Fourier-transform limited pulse duration was 3.1 fs in both cases. A two-point beam pointing stabilization system ensures stable coupling of the OPCPA beam into the HCF over time (not shown in the block diagram of figure 5).

The results of this subsection show that both methods are a viable option to generate near-single-cycle pulses with high average power and high repetition rate in the pulse energy range of a few-hundred μJ. The MPSC method is cost-effective and simple to implement. The HCF provides a cleaner spatio-temporal distribution, leading to less degradation of the peak intensity. The HCF is more sensitive to the input beam pointing fluctuations. However, if these fluctuations are minimized by relatively standard beam pointing stabilization methods, the output of the HCF provides a source fixed in space for applications (i.e. no translation of beam pointing instabilities to particular applications). In general, which method is more appropriate depends on the requirements of each particular application. In this case, the HCF provided a robust source of near-single-cycle pulses with a well-defined position in space and high quality beam profile, and it was the method of choice for applications utilizing post-compressed pulses. In future experiments,

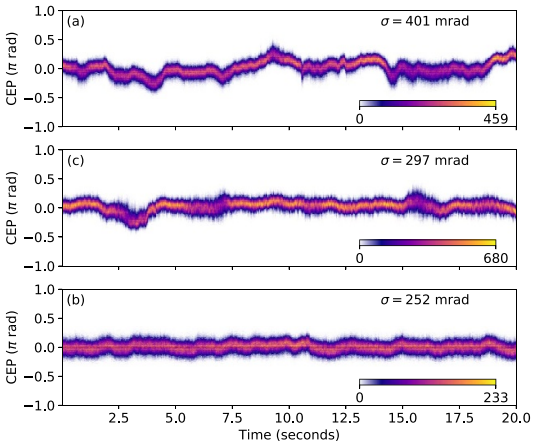

Figure 12. Single-shot characterization of the CEP in a stereo-ATI experient (a) CEP of the amplified pulses when the oscillator is CEO-frequency locked, and there is no additional CEP stabilization after the OPCPA. (b) CEP of the amplified pulses when a feedback signal is generated from an f-2f measurement and the CEP is measured out of loop using the stereo ATI. (c) CEP of the amplified pulses when a feedback signal is generated with the stereo ATI measurement. Adapted with permission from [175] © The Optical Society.

compression of the OPCPA pulses in a MPC will also be tested as an alternative method, following up on a recently published proof-of-principle test [105].

2.3.3. CEP stability

As pointed out in section 1.2, controlling the CEP of the amplified pulses is essential for confining the XUV emission during the HHG process to a single half-cycle of the driving field. The seed pulses incident on the first OPA stage have a repetition rate of 80 MHz and a phase-slip from pulse-to-pulse of $\pi/2$ rad. However, the pump pulses entering the OPA stages have a repetition rate of 100 kHz. That implies that, every 800 pulses, one pulse in the oscillator pulse train is amplified. It also implies that in theory, the amplified pulses all carry the same CEP. Of course, in practice, the CEP can slightly change over time due to small variations in the amplification conditions (pump energy fluctuations, small changes in the spatial and temporal overlap, air fluctuations, etc). In order to measure and stabilize the CEP after amplification in the OPCPA over a long time scale, the phase stability of the spectral fringes from an f-2f interferometer [172] was studied. The spectral fringes were acquired with a spectrometer (HR4000, Ocean Optics Inc.) and processed with a Python-based software to generate a control signal that was used as feedback signal sent to the modulation input of the CEO-frequency stabilization unit in the oscillator. When the CEP of the OPCPA pulses is actively stabilized in this way, the measured residual phase noise measured over a time span of 40 min was characterized by a standard deviation of 195 mrad [132]. However, each value of the CEP in this measurement is the result of integration over 100 laser shots, due to the minimum integration time in the spectrometer. Therefore, high frequency noise is effectively washed out. Taking into account as well the data processing time, the feedback loop had a bandwidth of 110 Hz.

To properly characterize the CEP stability on a single-shot basis, a stereo above threshold ionization (stereo-ATI) experiment [173] was performed. During the stereo-ATI measurement, xenon atoms were ionized by the strong field of the few-cycle laser pulse. The photoelectron kinetic energy distribution was measured in two different time of flight (TOF) spectrometers located on opposite sides along the laser polarization direction. From the asymmetry in the number of photoelectrons flying to one or the other spectrometer measured in two different regions of the kinetic energy spectra, the value of the CEP can be unambiguously determined [173, 174]. In this experiment, the OPCPA pulses were nonlinearly compressed in the HCF compressor. 30 μJ pulses were focused into the vacuum chamber containing the spectrometers to ionize the xenon atoms. The signals were analyzed in real time (within 300 ns) and in some cases (see below) used as a second feedback signal for the CEO-frequency locking electronics in the oscillator. It is worth noting that this technique allowed measuring the CEP of individual pulses at the full repetition rate of 100 kHz and therefore represents a conclusive method to determine the stability of the CEP at this high repetition rate. More details about the experiment can be found in [175]. Figure 12 shows a comparison between the results of stereo-ATI CEP measurements performed under three different conditions: (a) oscillator CEO-frequency locked, no additional feedback, (b) oscillator CEO-frequency locked and additional feedback with a signal generated in an f-2f interferometer and (c) oscillator CEO-frequency locked

and additional feedback with a signal generated from the stereo-ATI measurement. In all cases the CEP was measured during a time span of 20 s (2 million laser shots). In the first measurement, shown in figure 12(a), the CEP of the amplified pulses was evaluated when the oscillator was CEO-frequency locked but no additional feedback was applied to compensate for the changes over time in the CEP of the amplified pulses. The measurement essentially shows that there is no substantial high frequency noise, and the most important instability that needs to be corrected is the slow drift of the CEP that takes place over a few seconds. The second measurement, shown in figure 12(b), corresponds to an out-of-loop measurement of the residual phase noise performed with the stereo-ATI, when the CEP is stabilized utilizing the signal from an f-2f interferometer. In this case, the standard deviation of the residual phase noise is almost 300 mrad, and translates to 284 mrad when the intrinsic uncertainty of the stereo-ATI measurement is taken into consideration. The results show that stabilization of the CEP of the amplified pulses using an f-2f interferometer to generate a feedback signal is perfectly adequate for this system. The third measurement shown in figure 12(c) corresponds to the CEP when a feedback signal generated from the stereo-ATI measurement is used to stabilize the CEP. The measured standard deviation of the residual phase noise is even lower, 252 mrad which translates into 235 mrad when the intrinsic uncertainty of the stereo-ATI measurement is taken into account. However, this is an in-loop measurement, so the residual phase noise could be underestimated. The large correction bandwidth of the stereo-ATI electronics allows correcting the phase noise at high frequencies. A frequency analysis of the measured CEP shows that the phase noise is significantly reduced over almost the full spectral range (up to 50 kHz).

The high power, high repetition rate OPCPA in the NIR presented in this section generates CEP-stable sub-7 fs pulses with 190 μJ at a repetition rate of 100 kHz or alternatively CEP-stable sub-4 fs pulses with up to 95 μJ at 100 kHz after compression in a HCF [176]. This system offers all the required characteristics to drive an attosecond pump-probe beamline with electron-ion coincidence detection. In the following section, an attosecond pump-probe beamline design to work with this OPCPA system will be presented. In addition, results from pump-probe experiments designed to characterize XUV attosecond pulses, and first proof-of-principle results with a ReMi will be shown.

3. Attosecond pump-probe spectroscopy with high acquisition rate

The high power, high repetition rate light sources introduced in section 2 have enabled the generation of XUV attosecond pulses at high repetition rate via HHG [78, 80, 153, 177]. Depending on the pulse energy and duration, it is sometimes necessary to implement a tight focusing geometry, in which case phase matching can be achieved by properly scaling the gas pressure [178, 179] in the generation medium. The tight focusing geometry has been successfully implemented to generate high-order harmonics from OPCPAs and post-compressed Yb-CPAs [180–182] and also from Yb-CPAs [183–185]. In fact, in some of these experiments, CEP-dependent XUV emission has been observed [180, 186], showing the possibility of generating IAPs. Some of these high repetition rate XUV sources have been implemented for different applications such as time- and angle-resolved photoemission spectroscopy in solids [187], coherent diffractive imaging [188], or attosecond pump-probe spectroscopy [79]. In particular, high repetition rate OPCPAs and post-compressed Yb-CPAs are being implemented in attosecond pump-probe experiments with coincidence detection of ions and photoelectrons [189–193].

In this section we introduce a beamline for XUV-NIR attosecond pump-probe experiments with electron-ion coincidence detection capabilities developed at the MBI and driven by the OPCPA system described in the previous section. First, the experimental apparatus will be described. Next, results on the generation and characterization of trains of attosecond pulses and IAPs will be presented. And finally, some results on a proof-of-principle attosecond pump-probe experiment will be shown involving the detection of electrons and ions in coincidence with a ReMi.

3.1. Attosecond pump-probe setup

Figure 13(a) is a block diagram representing the full experimental setup. The block OPCPA contains the entire system introduced in section 2.3, including the optional stage for nonlinear pulse post-compression. Before entering the pump-probe setup, the pointing of the high power NIR beam is stabilized with a two-point stabilization system. In the attosecond interferometer the NIR pulses are split, the XUV light is generated in one of the arms of the interferometer, and subsequently XUV and NIR pulses are recombined with a variable delay. Figure 13(b) shows the interferometer in more detail, consisting of several interconnected vacuum chambers. The amplified NIR pulses enter the splitting chamber through a 0.5 mm thick, broadband anti-reflection-coated window and are split by a 1 mm thick beam splitter with a broadband coating introducing minimum GDD over the full bandwidth of the NIR pulses. The beam splitter transmits 80% of the incident power, which is used for XUV generation. These pulses are focused by a

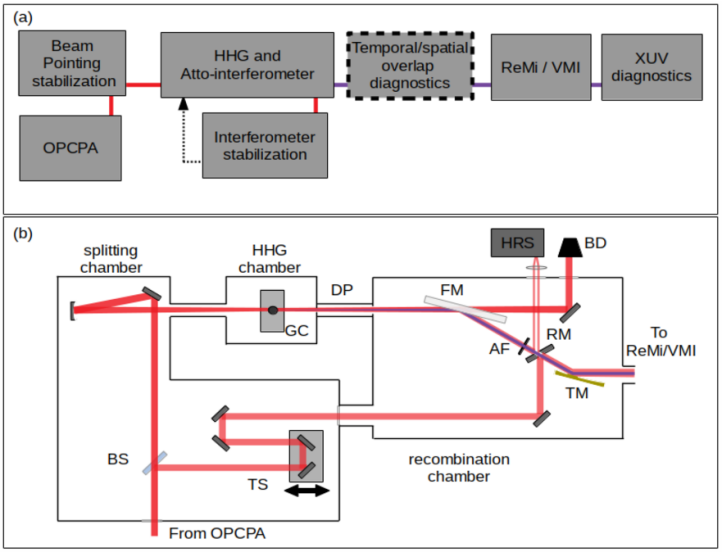

Figure 13. (a) Block diagram of the full experimental setup. The solid lines represent the beams (red: NIR, violet: XUV or both), while the dashed arrow represents an electronic feedback signal. The block surrounded by dashed lines indicates the availability of diagnostics tools that are not used during photoionization experiments. (b) Sketch of the attosecond interferometer and high harmonic generation stage. The NIR beam is represented in red and the XUV beam in violet. BS: beam splitter. TS: translation stage. GC: gas cell. DP: differential pumping stage. FM: filter mirror. AF: aluminium filter. RM: recombination mirror. TM: toroidal mirror. BD: beam dump. HRS: high resolution NIR spectrometer.

spherical mirror with a focal length of 0.5 m into a cylindrical gas cell contained in the HHG chamber. Unless otherwise specified, all mirrors are silver-coated with a thin dielectric multi-layer coating on top that enhances the reflectivity with minimum GDD over the full bandwidth. During the preparation of the experiments, the pulse characterization with the SEA-F-SPIDER takes into account all dispersion in the optical path up to the point where the XUV light is generated, so as to obtain the best compression during the HHG process. The gas cell for the HHG is mounted on an *XYZ* translation stage that allows precise positioning of the cell. The cell has a diameter of 2 mm and includes two 1 mm diameter holes facing each other for the beam to enter and exit the cell. In order to maintain the gas pressure in the cell without introducing significant gas load to the vacuum chamber, the holes are first covered with aluminium tape and subsequently input and output holes are drilled in the tape with the laser beam, thus keeping the size of the holes to a minimum. Under typical conditions generating harmonics in Ar or Kr, the backing pressure in the cell is in the order of 50–100 mbar.

After harmonic generation the XUV and the remaining NIR driver beam go through a differential pumping stage before entering the recombination chamber. In the recombination chamber the beams are reflected at a grazing incidence angle of 15° with respect to the plane of the mirror on a dielectrically coated mirror that allows removing about 80% of the NIR light while reflecting about 45% of the XUV light in the spectral range between 20 and 60 eV. The discarded NIR light is sent to a beam dump outside the vacuum chamber to avoid creating a significant heat load inside the vacuum chamber. After the filter mirror, a 200 nm thick metal filter (made of aluminium for all the results shown below) is placed in the path of the beams. The metal filter has two important functions. First, it completely blocks the remaining NIR light that co-propagates with the XUV, so that the only NIR light reaching the interaction region in the experiment originates from the NIR probe arm, with a controlled delay. Second, it introduces a negative GDD for the XUV light that allows partially compensating the positive chirp acquired during the HHG process, thus compressing the XUV pulses [194]. Note that, without the dielectric filtering mirror, the metal filter would melt at the average power level given by the output of the OPCPA. After the metal filter, the XUV beam travels through a hole in the recombination mirror.

The remaining 20% of the total power from the NIR OPCPA reflected off the beam splitter in the splitting chamber is sent through a 0.5 mm thick fused silica plate (not shown) at Brewster angle (for approximate dispersion matching of both arms of the interferometer) to a delay line with a translation stage (SLC-175S-HV, SmarAct GmbH). The translation stage allows controlling the XUV-NIR pump-probe delay with attosecond precision. After the delay line, a motorized iris (not shown) is used to control the NIR intensity and subsequently the NIR probe pulses traverse a 0.5 mm thick broadband anti-reflection coated window and reach the recombination chamber. In the recombination chamber the NIR beam is focused in vacuum (focusing optics and focused beam not shown) at a position equivalent to the XUV generation point

in the XUV-pump arm. Next, the NIR pulses are sent to the recombination mirror, where the outer part of the beam is reflected to travel colinearly with the XUV beam. Both beams are then directed to a gold-coated toroidal mirror and from there to the detector chamber, where the photoionization experiments take place. The toroidal mirror images the plane where the harmonics are generated (and where the NIR pulses are focused in the NIR-probe arm) to the interaction point of the experiment. The object distance in the imaging system is 1.25 m.

Note from figure 13 that the center of the NIR beam from the NIR-probe arm, which is not reflected by the recombination mirror, traverses this mirror and is directed into a high resolution spectrometer outside the chamber. The additional beam incident on the spectrometer that is shown in the figure originates from the XUV pump arm. In order to preserve a small portion of the NIR driver beam, the aluminium filter is mounted on a fused silica glass plate (with a hole in the center, where the filter is located). In this way, the outer part of the remaining NIR beam from the XUV pump arm is reflected on the back of the recombination mirror and directed toward the high resolution spectrometer. Since the two beams reaching the spectrometer travel through significantly different optical paths (i.e. the beam from the XUV pump arm travels through the fused-silica glass plate), their interference creates a modulation in the detected spectrum. The modulation frequency is easily detected in the Fourier domain and the phase corresponding to the modulation frequency can be detected in real time in order to monitor changes in the optical path difference. In this way, a feedback signal is generated that acts on the translation stage for stabilization of the XUV-NIR pump-probe delay in the experiment. This stabilization systems allows performing pump-probe experiments while maintaining a residual jitter characterized by a standard deviation below 100 as over several days.

Before entering the detector chamber, the XUV pump and the NIR probe pulses travel through an intermediate chamber that serves both as differential pumping stage and as a diagnostic for the temporal and spatial overlap of the pulses. In order to diagnose the overlap, a movable mirror is introduced in the path of the beams and, upon reflection off this mirror, the pulses exit the chamber through a viewport. Since the XUV light is absorbed in the viewport, the aluminium filter is removed from the XUV-pump arm and the co-propagating NIR beam is used for this analysis instead. A charge coupled device sensor (CCD) is utilized to monitor the spatial overlap at the focal plane. The overlap can be corrected by tilting the recombination mirror, which sits on a motorized mirror mount with piezoelectric actuators. To find the temporal XUV/NIR overlap, the CCD is replaced by a commercial NIR spectrometer. The delay is varied until a delay-dependent modulation appears in the spectrum. Subsequently, the delay is varied so that the frequency of the modulation decreases, since the frequency of this spectral modulation is proportional to the optical path difference. When the modulation is minimal, the spectrometer is once again replaced by the CCD. At this point, a Python-based program performs a scan that acquires images of the overlapped beams as a function of delay, from whose interference signal, upon spatial integration, an autocorrelation signal of the pulses can be derived and the time overlap identified. Once the spatial and temporal overlap have been optimized, the aluminium filter is placed once again in the XUV-pump arm, and the steering mirror in the overlap diagnostics chamber removed, so that the XUV and NIR beams reach the detection chamber.

The actual experiment takes place in the chamber containing the detector, which can be a velocity map imaging (VMI) spectrometer or a ReMi. In both cases, the pump-probe pulse sequence interacts with the atoms or molecules to be studied at the center of this chamber, and the momentum distributions of the resulting photoions and/or photoelectrons are detected. Behind the detector, the XUV photon flux can be measured with a photodiode (AXUV100G, Opto Diode), which can be moved into the path of the beam. Finally, the XUV spectrum can be measured in a spectrometer consisting of a flat-field grating, a microchannel plate (MCP)—phosphor screen assembly, and a CCD that images the phosphor screen from outside the chamber through a viewport. A thorough description of the attosecond pump-probe setup and XUV spectrometer can be found in Osolodkov *et al* [195].

3.2. Attosecond pulses at 100 kHz

In a first set of XUV-NIR pump-probe experiments, the temporal structure of the XUV harmonic emission was studied for two distinct XUV generation conditions: HHG driven by ≈7 fs pulses directly from the OPCPA, and by sub-4 fs pulses after nonlinear compression in the HCF setup. In both cases, the pump-probe sequence was used to ionize a gas of atoms and the resulting photoelectron momentum distribution was measured with a VMI spectrometer.

The VMI spectrometer utilized a 50 μm nozzle directly in the repeller electrode of the electrostatic-lens assembly in order to reach high densities in the interaction region, typically located a few hundred μm away from the repeller [196]. The electrostatic lens assembly projects the three-dimensional photoelectron momentum distribution onto a two-dimensional detector (MCP-phosphor screen assembly + CCD camera outside the chamber). A VMI image was acquired for each delay between the XUV and NIR pulses. Given

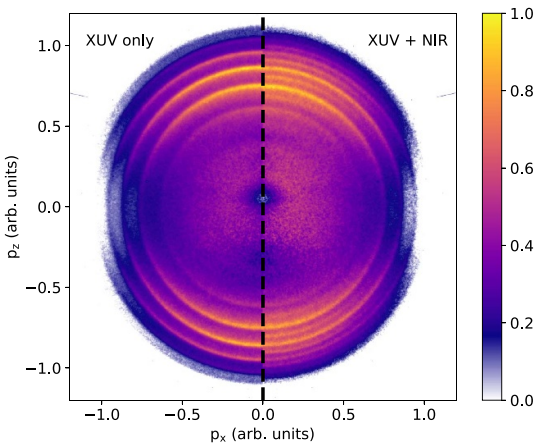

Figure 14. Two-dimensional projection of the three-dimensional photoelectron momentum distribution measured with the VMI. The image is cut in two halves indicated by a black dashed line in the vertical direction: the left half corresponds to ionization of Ar atoms by XUV light and the right half to ionization of Ar atoms by XUV light in the presence of a NIR dressing field. The polarizaton direction is parallel to p_z. Data from [195].

that the polarization vectors of both beams were parallel to the plane of the detector, an Abel inversion could be performed to retrieve the three-dimensional momentum distribution from its two-dimensional projection. Figure 14 shows two experimental half-images: XUV-only on the left, XUV + NIR on the right. In this case, the HHG process was driven by 7 fs pulses from the OPCPA.

The *xy* coordinates in figure 14 represent momentum while the colorscale indicates the number of counts (normalized to the maximum). The clear ring structure on the left side of the image corresponds to ionization of Ar by different harmonics in the XUV spectrum. In contrast, the right side of the image illustrates the influence of the NIR field: when ionization occurs in the presence of a moderate NIR field (intensity <1 TW cm^{-2}), additional rings appear in between the rings corresponding to the harmonics. These additional rings (sidebands) can be interpreted as coming from two different processes: absorption of one XUV photon (harmonic q) plus one NIR photon, or absorption of one XUV photon (harmonic $q+2$) accompanied by stimulated emission of one NIR photon. The two processes lead to the same final kinetic energy and interfere. This interference results in oscillations in the sideband intensity as the delay between the XUV and NIR is changed. The sideband oscillations can be utilized to retrieve the temporal structure of the harmonic emission [26].

However, when the HHG process is driven by near-single-cycle pulses and in the limit that only one isolated attosecond XUV pulse is produced, the XUV spectral modulation (i.e. the harmonic structure) vanishes, as well as the corresponding sidebands. Both two-color XUV + NIR ionization using APT, where sidebands are observed, or IAP, where they are not, can be analyzed from a more general point of view. In both cases the probability amplitude ($\tilde{a} = \tilde{a}(\vec{p}, \tau)$) for a transition to the continuum with final photoelectron momentum $\vec{p}$ is given in atomic units by [197]:

$$\tilde{a} = -i \int_{-\infty}^{\infty} dt \tilde{d} \tilde{E}(t-\tau) e^{i[(W+\mathrm{IP})t - \int_t^{\infty} dt' (\vec{p}\cdot\vec{A}(t') + \frac{1}{2}A(t')^2]} \tag{5}$$

where τ is the pump-probe delay, $\tilde{E}$ is the complex electric field amplitude of the XUV pulse, $\tilde{d} = \tilde{d}_{\vec{p}+\vec{A}(t)}$ represents the complex dipole transition matrix element for the transition connecting the ground state and the final state in the continuum, IP is the ionization potential of the ionized atom, $\vec{p} + \vec{A}(t)$ is the instantaneous kinetic momentum, and $W = p^2/2$ is the measured photoelectron kinetic energy. By selecting photoelectrons emitted in a particular direction with respect to the polarization direction, a map of the number of photoelectrons as a function of kinetic energy and XUV-NIR pump-probe delay can be constructed, which can be identified as a frequency-resolved optical gating (FROG) trace [198] in which the photoelectron wave packet $\tilde{d}_{\vec{p}+\vec{A}}\tilde{E}$ is the unknown pulse and the gate function is given by a pure phase modulation. If it is possible to approximate the momentum $\vec{p}$ in the phase modulation term by its value at the center of the distribution (center momentum approximation), the retrieval methods developed for optical pulses can be applied to reconstruct the XUV and NIR pulses, in a technique dubbed FROG for Complete Reconstruction of Attosecond Bursts or FROG-CRAB [199].

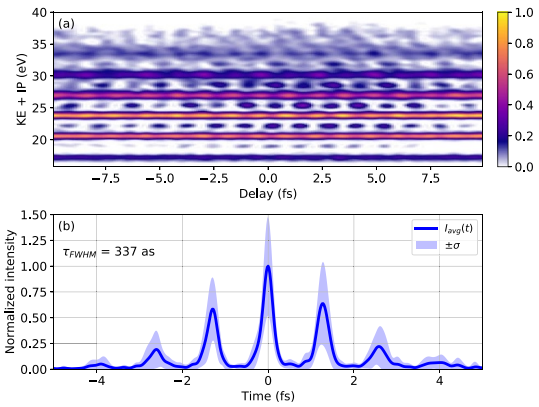

Figure 15. (a) Photoelectron kinetic energy along the polarization direction as a function of XUV-NIR pump-probe delay. (b) Retrieved train of attosecond pulses. Data from [195].

3.2.1. Retrieval of APTs

In a first experiment, the pump-probe beamline was driven by the output of the OPCPA without implementation of nonlinear pulse post-compression. In addition, although the CEO-frequency was locked in the oscillator, no additional feedback loop was implemented after the OPA stages for the compensation of CEP drifts. XUV light was generated by focusing the driving NIR pulses into the gas cell in the HHG chamber to an approximate intensity of 200 TW cm^{-2}, while the gas cell was filled with Kr at a pressure of 70 mbar. The resulting XUV emission was characterized by a clear harmonic structure, whose spectrum extends from 15.6 eV (aluminium low energy transmission edge) to approximately 40 eV. The XUV photon flux measured after the VMI spectrometer amounted to 2.2×10^{11} photons s^{-1} or 2.2×10^{6} photons/pulse. In the detector chamber Ar atoms were ionized by the XUV radiation in the presence of the NIR probe field, which in this case had an approximate intensity of 50 GW cm^{-2}. Figure 15(a) shows the photoelectron kinetic energy distribution along the polarization axis after processing the raw data as explained before. It was observed that implementation of standard FROG-CRAB algorithms for the retrieval of the XUV pulses from the trace of figure 15(a) led to a reconstructed pulse train structure very close to the corresponding Fourier-transform limit of the XUV spectrum. The reconstructed temporal shape was dominated by a single pulse with weak satellites, which is rather unexpected for a ~7 fs NIR driver pulse. This is reminiscent of the known coherent artifact problem in the retrieval of optical pulses when the pulses are changing from shot-to-shot [200]. In this case, given that the driving pulses for the HHG process consist of less than three optical cycles, the changes in the CEP over time introduce small, but non-negligible changes to the XUV pulse train that affect the pulse reconstruction algorithms. To circumvent this problem, the utilized FROG-CRAB algorithm was modified in the following manner: instead of considering a single pair of XUV-NIR pulses, the algorithm included an ensemble of XUV-NIR pulse pairs [201]. In this case, a set of XUV and a set of NIR pulses were retrieved. Figure 15(b) shows the average of the reconstructed APT set. The average APT was characterized by the presence of at least 7 attosecond pulses separated by half the period of the NIR optical cycle and with a duration below 500 as. The main pulse in the train had an average duration of (337 $\pm$ 108) as. The algorithm also retrieved an average NIR pulse with a duration of 7.2 fs FWHM [195].

3.2.2. Attosecond electron streaking at 100 kHz

In a second pump-probe experiment with the VMI spectrometer, the full system in figure 5 was utilized, generating CEP-stable, sub-4 fs NIR pulses. Under these conditions, i.e. when the pulse duration approaches the single-cycle limit, the harmonic emission changes substantially when the CEP undergoes a $\pi/2$ shift, leading alternatively to a single dominant attosecond XUV pulse, or a pair of attosecond XUV pulses with similar intensities. This manifests itself particularly in the cut-off region of the XUV spectrum, which alternates between a smooth (single pulse) or modulated (pair of pulses) spectrum [34]. Therefore, prior to the beginning of the pump-probe experiment, the XUV spectrum was measured as a function of the CEP. The CEP stability of the amplified and post-compressed pulses was ensured by implementing a second feedback loop based on an f-2f interferometer, as described in section 2.3.3. Downstream from the point where the CEP was analyzed, the insertion into the beam path of one of the thin fused silica wedges used for pulse compression was varied in order to change the CEP. From the resulting map of XUV spectra as a function of wedge position, it is possible to determine the position around which the pulses are best compressed (highest peak intensity, thus highest XUV cut-off frequency) and, around this region, the position for which the cut-off region of the spectrum is smooth, suggesting the formation of an IAP. The

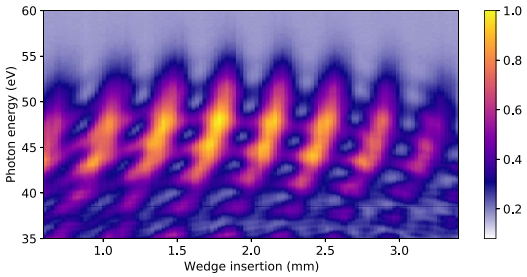

Figure 16. XUV spectra as a function of wedge insertion for HHG with a CEP-stable NIR driver. Adapted with permission from [176] © The Optical Society.

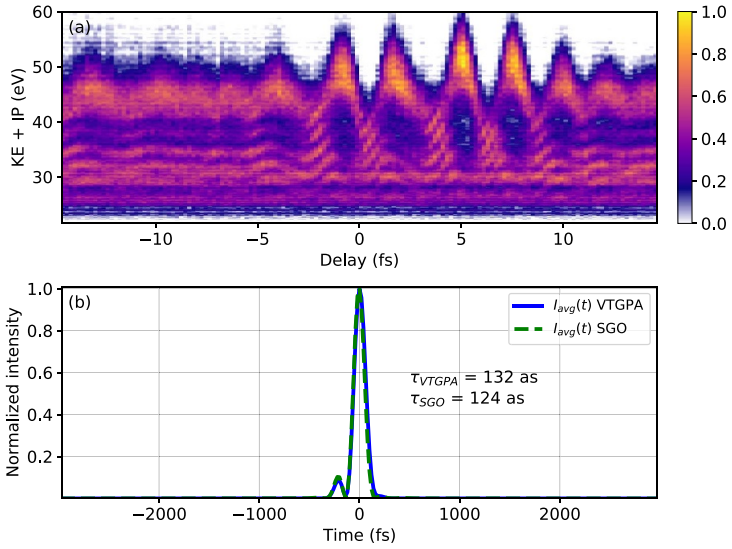

Figure 17. (a) Photoelectron kinetic energy distribution along the polarization direction as a function of XUV-NIR pump-probe delay. (b) Retrieved XUV pulses with the VTGPA and SGO methods. Adapted with permission from [176] © The Optical Society.

XUV light was generated by focusing the CEP-stable, near-single-cycle NIR pulses into the gas cell in the HHG chamber to an approximate intensity of 200 TW cm^{-2}. The cell was filled with Kr at a pressure of 70 mbar. Figure 16 shows XUV spectra as a function of the insertion of the thin fused silica wedge.

For the selected position of the wedge, the XUV spectrum extended to approximately 55 eV and the photon flux reaching the interaction region of the VMI spectrometer (measured with the XUV photodiode) was 10^{11} photons s^{-1} or 10^6 photons/pulse. In this experiment, Ne atoms were photoionized in the interaction region of the VMI spectrometer by the XUV light, in the presence of a dressing NIR field with an approximate intensity of 4.6 TW cm^{-2}. This higher intensity, compared to the previous experiment, is better suited to induce photoelectron streaking. Once again, the photoelectron kinetic energy spectra were reconstructed along the polarization direction. Figure 17(a) shows the measured spectra as a function of the XUV-NIR pump-probe delay. In this case, the photoelectron spectrum as a whole is shifted in energy depending on the value of the NIR vector potential at the moment when the photoelectron wave packet is launched into the continuum. This effect maps the NIR vector potential onto the photoelectron kinetic energy as a function of pump-probe delay [197, 202]. The resulting FROG-CRAB trace encodes information about both, the NIR and the XUV pulses, as can be deduced from equation (5). Once again, implementation of one of the standard pulse retrieval algorithms is not possible. The reason in this case is that the center momentum approximation cannot be applied because the condition $p_o \ll \Delta p$ is not satisfied, where p_o is the central momentum of the photoelectron distribution and Δp its bandwidth. An algorithm that circumvents the center momentum approximation, named Volkov-Transform Generalized Projection Algorithm or VTGPA [203] was implemented for the retrieval of the XUV and NIR pulses. In addition, an alternative approach was developed, based on the parametrizaton of the XUV spectral phase and implementation of a global optimization algorithm. This new algorithm named streaking global optimization was implemented for the pulse reconstruction as well. Further details about the analysis and the algorithm can be found in [176]. Figure 17(b) shows the retrieved pulses with both methods. The temporal structure of the XUV

radiation is characterized by a dominant pulse with a duration below 140 as, accompanied by weak satellite pulses (<1%) at ≈±1.35 fs, corresponding to XUV emission from different half-cycles of the NIR driving pulse during the HHG process. These results represent the first demonstration of IAPs at an unprecedented high repetition rate of 100 kHz.

3.3. Electron-ion coincidence detection with high acquisition rate

The results presented in the previous section show that the attosecond pump-probe beamline driven by a 100 kHz high power OPCPA is perfectly suited for performing attosecond pump-probe experiments with detection of electrons and ions in coincidence utilizing a ReMi. In this final subsection, the results of a proof-of-principle experiment with the ReMi are presented.

The experimental setup is identical to the one used in the experiments characterizing the XUV pulses, except that the VMI is replaced by a ReMi developed at the MBI [204]. In the interaction region of the ReMi, the pump-probe pulse sequence photoionizes the target atoms/molecules from a molecular beam that propagates perpendicular to the light propagation direction. A stack of annular electrodes (inside the chamber) and system of Helmholtz coils (outside the chamber) produce a static homogenenous electromagnetic field parallel to the polarization direction and perpendicular to both the light and molecular beam propagation directions, which guides the charged particles to two position-sensitive detectors located on opposite sides of the interaction region, along the field direction (detector axis). Both detectors consist of MCPs and delay-line anodes (DLD75-ions and HEX75-electrons, Roentdeck Handels GmbH) and allow recording the position where a particle hits the detector and the TOF from the interaction region to the detector. From this information, the momentum of the charged particle at its birth can be calculated.

In order to control the number of events per unit time, which as explained before has to be kept below a fraction of the light source repetition rate, the gas density in the molecular beam can be adjusted. The molecular beam is formed by adiabatic expansion of a gas through a nozzle into an evacuated chamber, a properly located skimmer within the zone of silence of the supersonic gas expansion, and one differential pumping stage separating the source chamber (into which the gas is released) from the interaction chamber of the ReMi. The molecular beam enters the interaction chamber through a ≈1 mm orifice, crosses the interaction region perpendicular to the light propagation direction, and exits the chamber through another ≈5 mm orifice into a dump chamber where the atoms/molecules in the beam are pumped out of the system. The dump chamber limits the increase of the pressure in the interaction chamber (typically below 10^{-9} mbars during operation). More details about the ReMi can be found in [204, 205].

As a proof-of-principle experiment showing the potential of the system, results on the photoionization of Ar atoms by a sequence of XUV-NIR pulses are presented below. The experiment was run under similar conditions to the experiment characterizing the APTs of section 3.2.1 (HHG in Kr using 7 fs pulses from the OPCPA). The data acquisition is triggered by a photoelectron. The TOF toward the two detectors and the position on the detectors are registered within a certain time window for all photoelectrons and ions respectively. Figure 18(a) shows a TOF spectrum of all ions detected during the experiment. The narrow strong peak close to 21 μs corresponds to singly charged Ar^+ ions from the molecular beam. This narrow peak is sitting on a broader pedestal that corresponds to the ionization of Ar atoms that were not discarded in the dump chamber and contribute to the background in the interaction chamber. Other peaks correspond to ionization of other background gases or ionization of Ar in the molecular beam by earlier XUV pulses (narrow peaks close to 1 and 11 μs). These events appear in the TOF spectrum when an ionization event happens, but the photoelectron is either not detected and hence, no trigger is activated, or it falls inside an already open acquisition window. In both cases, the ion is detected and appears in the acquisition window of a subsequent triggered event, since the duration of the acquisition window exceeds the inter-pulse spacing (10 μs). Given a particular triggered event of ionization of Ar that appears in the ion TOF (one electron and one Ar^+ ion detected) the probability that ionization of Ar happens for any other laser pulse different from the one that triggered the detection window, is simply the probability of ionization. In this case the probability of ionization is approximately 0.1 and therefore, the peaks appearing close to 11 and 1 μs are approximately 10% weaker than the peak appearing close to 21 μs. Notice that for the actual event rate the detection efficiencies of the detectors have to be taken into account, which in this case lowers the event rate to approximately 0.05 times the repetition rate of the laser.

From the TOF and the position on the detectors, and using the known information on the applied extraction fields, the three-dimensional momenta of the ions and electrons can be directly calculated. Figure 18(b) shows a slice through the three-dimensional momentum distribution of electrons correlated to the main peak in the ion TOF spectrum. The $p_x - p_z$ slice in the figure integrates events over all XUV-NIR pump-probe delays and includes photoelectrons with $|p_y| < 0.1$ a.u. Here p_z is parallel to the detector axis and the polarization direction. The empty straight line at $p_z \approx 0.1$ a.u. corresponds to a particular electron TOF for which the electron trajectories converge to a node and the spatial resolution decreases drastically

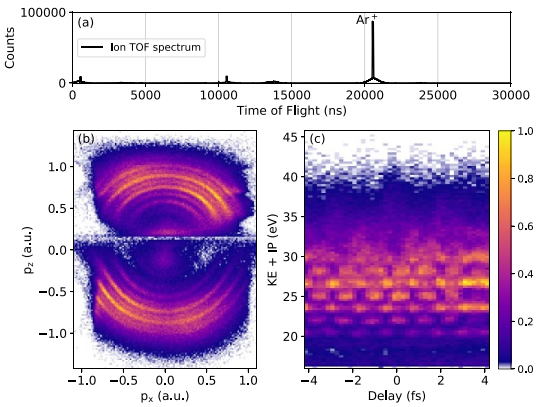

Figure 18. (a) TOF spectrum of ions detected with the ReMi. (b) Slice through the three-dimensional momentum distribution of photoelectrons correlated to the main peak in the ion TOF spectrum. The number of counts has been normalized to the maximum. (c) Kinetic energy spectrum as a function of XUV-NIR pump-probe delay for photoelectrons correlated to the main peak in the ion TOF spectrum and emitted along the laser polarization direction. The number of counts has been normalized to the maximum.

[204]. In figure 18(b), the strong rings correspond to ionization by particular harmonics. On top of that, the weaker rings in between clearly show sidebands resulting from two-color (XUV + NIR) transitions. Finally, figure 18(c) shows the kinetic energy spectrum of the photoelectrons corresponding to single ionization of Ar as a function of pump-probe delay. In this case, only photoelectrons emitted within a cone determined by $\sqrt{p_x^2 + p_y^2} < \tan(\theta) p_z$, with $\theta = 20°$ were considered. Figure 18(c) clearly shows the oscillations of the sidebands from which the XUV APT characteristics can be retrieved or properties of the target can be studied [206].

It is worth noting that in this first proof-of-principle experiment the event rate was limited to only 5 kHz, mostly due to limited pumping speed in the source chamber of the molecular beam. As a consequence the experiment ran for approximately two days. With recent modifications to the molecular beam setup, it has been possible to increase the event rate to the target value of 20 kHz for gas mixtures of N_2 in Ar or He, while the gas density in the molecular beam could still be considerably increased without overloading the source chamber. This opens the possibility to perform XUV-NIR pump-probe scans simultaneously for different species and, in particular, for low probability channels of molecules that undergo dissociation after photoionization, in a reasonable measurement time.

4. Summary and perspective

The latest developments in ultrafast laser amplifiers have enabled the generation of CEP-stable, few-cycle pulses with moderately high energies (several μJ to several mJ) at high repetition rates (hundreds of kHz) and unprecedented average powers exceeding 100 W. Two distinct approaches can be utilized to reach this aim: direct nonlinear compression of laser pulses from Yb-CPA systems and amplification of ultrashort pulses in OPCPA systems. Both approaches are already being implemented as driver laser systems for a new generation of attosecond pump-probe experiments in which charged particles produced during photoioniziation are detected in coincidence, thus providing access to information so far rarely available for this type of experiment: fully correlated momentum distributions of photoelectrons and ionic fragments, photoelectron distributions in the recoil frame of dissociating molecules, detection of different species simultaneously, etc. In particular, a high power OPCPA delivering CEP-stable, few-cycle and near-single-cycle pulses with high average power operating at 100 kHz has been presented. The system drives an attosecond pump-probe beamline with coincidence detection of ions and electrons. Furthermore, results on the generation of trains and single XUV pulses driven by this OPCPA and their characterization in pump-probe experiments have been presented. Moreover, results of a proof-of-principle experiment have been shown, in which ionization of Ar atoms by an XUV-NIR pump-probe sequence, is studied by the detection of photoelectrons and ions in coincidence utilizing a ReMi. It is anticipated that the capabilities of the new attosecond pump-probe beamline with coincidence detection at the MBI will offer a new, more detailed look into complex problems in attosecond molecular science [207] and will create opportunities to study fundamental concepts in quantum mechanics such as coherence and entanglement on ultrashort time scales [208–212]. Further developments of the light source will target a five-fold increase in the pulse energy of the OPCPA. The additional pulse energy will enable the generation of few-fs pulses in the deep ultraviolet

[213] which will be combined with attosecond XUV pulses. The implementation of short wavelength pulses for both the pump and the probe steps will reduce the complexity of the systems under study by avoiding distortions to the molecular potentials by a strong laser field and by limiting the involved transitions to one- or two-photon processes [214].

Data availability statement

The data that support the findings of this study are available upon reasonable request from the authors.

Acknowledgment

The authors acknowledge support from the European Union Horizon 2020 programme Laserlab Europe (638585 and 871124) and European Union Horizon 2020 Marie Curie ITN project ASPIRE (674960).

ORCID iDs

F J Furch https://orcid.org/0000-0002-8444-7162
T Witting https://orcid.org/0000-0002-2512-1840
M Osolodkov https://orcid.org/0000-0002-8328-5579

References

[1] Beaurepaire E, Merle J-C, Daunois A and Bigot J-Y 1996 Ultrafast spin dynamics in ferromagnetic nickel *Phys. Rev. Lett.* **76** 4250–3
[2] Filevich J *et al* 2005 Observation of a multiply ionized plasma with index of refraction greater than one *Phys. Rev. Lett.* **94** 035005
[3] Davis K M, Miura K, Sugimoto N and Hirao K 1996 Writing waveguides in glass with a femtosecond laser *Opt. Lett.* **21** 1729–31
[4] Hoy C L, Ferhanoglu O, Yildirim M, Kim K H, Karajanagi S S, Chan K M C, Kobler J B, Zeitels S M and Ben-Yakar A 2014 Clinical ultrafast laser surgery: recent advances and future directions *IEEE J. Sel. Top. Quantum Electron.* **20** 242–55
[5] Zewail A H 2000 Femtochemistry: atomic-scale dynamics of the chemical bond *J. Phys. Chem.* A **104** 5660–94
[6] Picqué N and Hänsch T W 2019 Frequency comb spectroscopy *Nat. Photon.* **13** 146–57
[7] Krausz F and Ivanov M 2009 Attosecond physics *Rev. Mod. Phys.* **81** 163
[8] Niikura H, Légaré F, Hasbani R, Bandrauk A D, Ivanov M Y, Villeneuve D M and Corkum P B 2002 Sub-laser-cycle electron pulses for probing molecular dynamics *Nature* **417** 917–22
[9] Baker S, Robinson J S, Haworth C A, Teng H, Smith R A, Chirilă C C, Lein M, Tisch J W G and Marangos J P 2006 Probing proton dynamics in molecules on an attosecond time scale *Science* **312** 424–7
[10] Shafir D, Soifer H, Bruner B D, Dagan M, Mairesse Y, Patchkovskii S, Ivanov M Y, Smirnova O and Dudovich N 2012 Resolving the time when an electron exits a tunnelling barrier *Nature* **485** 343–6
[11] Beaulieu S *et al* 2017 Attosecond-resolved photoionization of chiral molecules *Science* **358** 1288–94
[12] Makos I *et al* 2020 A 10-gigawatt attosecond source for non-linear XUV optics and XUV-pump-XUV-probe studies *Sci. Rep.* **10** 3759
[13] Major B *et al* 2020 Propagation-assisted generation of intense few-femtosecond high-harmonic pulses *J. Phys. Photonics* **2** 034002
[14] Drescher M, Hentschel M, Kienberger R, Uiberacker M, Yakovlev V, Scrinzi A, Westerwalbesloh T, Kleineberg U, Heinzmann U and Krausz F 2002 Time-resolved atomic inner-shell spectroscopy *Nature* **419** 803–7
[15] Uiberacker M *et al* 2007 Attosecond real-time observation of electron tunnelling in atoms *Nature* **446** 627–32
[16] Sansone G *et al* 2010 Electron localization following attosecond molecular photoionization *Nature* **465** 763–6
[17] Gruson V *et al* 2016 Attosecond dynamics through a Fano resonance: monitoring the birth of a photoelectron *Science* **354** 734–8
[18] Goulielmakis E *et al* 2010 Real-time observation of valence electron motion *Nature* **466** 739–43
[19] Kaldun A *et al* 2016 Observing the ultrafast buildup of a Fano resonance in the time domain *Science* **354** 738–41
[20] Drescher L, Reitsma G, Witting T, Patchkovskii S, Mikosch J and Vrakking M J J 2019 State-resolved probing of attosecond timescale molecular dipoles *J. Phys. Chem. Lett.* **10** 265–9
[21] Lucchini M, Sato S A, Ludwig A, Herrmann J, Volkov M, Kasmi L, Shinohara Y, Yabana K, Gallmann L and Keller U 2016 Attosecond dynamical Franz–Keldysh effect in polycrystalline diamond *Science* **353** 916–9
[22] McPherson A, Gibson G, Jara H, Johann U, Luk T S, McIntyre I A, Boyer K and Rhodes C K 1987 Studies of multiphoton production of vacuum-ultraviolet radiation in the rare gases *J. Opt. Soc. Am.* B **4** 595–601
[23] Ferray M, L'Huillier A, Li X F, Lompre L A, Mainfray G and Manus C 1988 Multiple-harmonic conversion of 1064 nm radiation in rare gases *J. Phys. B: At. Mol. Opt. Phys.* **21** L31–35
[24] Schafer K J, Yang B, DiMauro L F and Kulander K C 1993 Above threshold ionization beyond the high harmonic cutoff *Phys. Rev. Lett.* **70** 1599–602
[25] Corkum P B 1993 Plasma perspective on strong field multiphoton ionization *Phys. Rev. Lett.* **71** 1994–7
[26] Paul P M, Toma E S, Breger P, Mullot G, Augé F, Balcou P, Muller H G and Agostini P 2001 Observation of a train of attosecond pulses from high harmonic generation *Science* **292** 1689–92
[27] Kung A H, Young J F and Harris S E 1973 Generation of 1182-Å radiation in phase-matched mixtures of inert gases *Appl. Phys. Lett.* **22** 301–2
[28] Rundquist A, Durfee C G, Chang Z, Herne C, Backus S, Murnane M M and Kapteyn H C 1998 Phase-matched generation of coherent soft x-rays *Science* **280** 1412–5
[29] Mairesse Y *et al* 2003 Attosecond synchronization of high-harmonic soft x-rays *Science* **302** 1540–3
[30] Kazamias S and Balcou P 2004 Intrinsic chirp of attosecond pulses: single-atom model versus experiment *Phys. Rev.* A **69** 063416
[31] Isinger M *et al* 2017 Photoionization in the time and frequency domain *Science* **358** 893–6

[32] Neidel C et al 2013 Probing time-dependent molecular dipoles on the attosecond time scale Phys. Rev. Lett. 111 033001
[33] Krause J L, Schafer K J and Kulander K C 1992 High-order harmonic generation from atoms and ions in the high intensity regime Phys. Rev. Lett. 68 3535–8
[34] Baltuška A et al 2003 Attosecond control of electronic processes by intense light fields Nature 421 611–5
[35] Kienberger R et al 2004 Atomic transient recorder Nature 427 817–21
[36] Corkum P B, Burnett N H and Ivanov M Y 1994 Subfemtosecond pulses Opt. Lett. 19 1870–2
[37] Chang Z 2004 Single attosecond pulse and XUV supercontinuum in the high-order harmonic plateau Phys. Rev. A 70 043802
[38] Chang Z 2005 Chirp of the single attosecond pulse generated by a polarization gating Phys. Rev. A 71 023813
[39] Sansone G et al 2006 Isolated single-cycle attosecond pulses Science 314 443–6
[40] Oishi Y, Kaku M, Suda A, Kannari F and Midorikawa K 2006 Generation of extreme ultraviolet continuum radiation driven by a sub-10-fs two-color field Opt. Express 14 7230–7
[41] Pfeifer T, Gallmann L, Abel M J, Neumark D M and Leone S R 2006 Single attosecond pulse generation in the multicycle-driver regime by adding a weak second-harmonic field Opt. Lett. 31 975–7
[42] Takahashi E J, Lan P, Mücke O D, Nabekawa Y and Midorikawa K 2010 Infrared two-color multicycle laser field synthesis for generating an intense attosecond pulse Phys. Rev. Lett. 104 233901
[43] Pfeifer T, Jullien A, Abel M J, Nagel P M, Gallmann L, Neumark D M and Leone S R 2007 Generating coherent broadband continuum soft-x-ray radiation by attosecond ionization gating Opt. Express 15 17120–8
[44] Kim K T, Zhang C, Ruchon T, Hergott J-F, Auguste T, Villeneuve D M, Corkum P B and Quéré F 2013 Photonic streaking of attosecond pulse trains Nat. Photon. 7 651–6
[45] Chen M-C et al 2014 Generation of bright isolated attosecond soft x-ray pulses driven by multicycle midinfrared lasers Proc. Natl Acad. Sci. 111 E2361–7
[46] Nisoli M, De Silvestri S, Svelto O, Szipöcs R, Ferencz K, Spielmann C, Sartania S and Krausz F 1997 Compression of high-energy laser pulses below 5 fs Opt. Lett. 22 522–4
[47] Ullrich J, Moshammer R, Dorn A, Dörner R, Schmidt L and Schmidt-Böcking H 2003 Recoil-ion and electron momentum spectroscopy: reaction-microscopes Rep. Prog. Phys. 66 1463–545
[48] Stert V, Radloff W, Schulz C P and Hertel I V 1999 Ultrafast photoelectron spectroscopy: femtosecond pump-probe coincidence detection of ammonia cluster ions and electrons Eur. Phys. J. D 5 97–106
[49] Mikosch J and Patchkovskii S 2013 Coincidence and covariance data acquisition in photoelectron and -ion spectroscopy. I. Formal theory J. Mod. Opt. 60 1426–38
[50] Mikosch J and Patchkovskii S 2013 Coincidence and covariance data acquisition in photoelectron and -ion spectroscopy. II. Analysis and applications J. Mod. Opt. 60 1439–51
[51] Sabbar M, Heuser S, Boge R, Lucchini M, Gallmann L, Cirelli C and Keller U 2014 Combining attosecond XUV pulses with coincidence spectroscopy Rev. Sci. Instrum. 85 103113
[52] Cattaneo L, Vos J, Bello R Y, Palacios A, Heuser S, Pedrelli L, Lucchini M, Cirelli C, Martín F and Keller U 2018 Attosecond coupled electron and nuclear dynamics in dissociative ionization of H_2 Nat. Phys. 14 733–8
[53] Vos J, Cattaneo L, Patchkovskii S, Zimmermann T, Cirelli C, Lucchini M, Kheifets A, Landsman A S and Keller U 2018 Orientation-dependent stereo Wigner time delay and electron localization in a small molecule Science 360 1326–30
[54] Stockman M I, Kling M F, Kleineberg U and Krausz F 2007 Attosecond nanoplasmonic-field microscope Nat. Photon. 1 539–44
[55] Locher R, Castiglioni L, Lucchini M, Greif M, Gallmann L, Osterwalder J, Hengsberger M and Keller U 2015 Energy-dependent photoemission delays from noble metal surfaces by attosecond interferometry Optica 2 405–10
[56] Emons M, Steinmann A, Binhammer T, Palmer G, Schultze M and Morgner U 2010 Sub-10-fs pulses from a MHz-NOPA with pulse energies of 0.4 μJ Opt. Express 18 1191–6
[57] Rothhardt J et al 2010 High average and peak power few-cycle laser pulses delivered by fiber pumped OPCPA system Opt. Express 18 12719–26
[58] Hädrich S et al 2016 Energetic sub-2-cycle laser with 216 W average power Opt. Lett. 41 4332–5
[59] Eidam T, Hanf S, Seise E, Andersen T V, Gabler T, Wirth C, Schreiber T, Limpert J and Tünnermann A 2010 Femtosecond fiber CPA system emitting 830 W average output power Opt. Lett. 35 94–96
[60] Stark H, Buldt J, Müller M, Klenke A and Limpert J 2021 1 kW, 10 mJ, 120 fs coherently combined fiber CPA laser system Opt. Lett. 46 969–72
[61] Müller M, Aleshire C, Klenke A, Haddad E, Légaré Fçois, Tünnermann A and Limpert J 2020 10.4 kW coherently combined ultrafast fiber laser Opt. Lett. 45 3083–6
[62] Giesen A and Speiser J 2007 Fifteen years of work on thin-disk lasers: results and scaling laws IEEE J. Sel. Top. Quantum Electron. 13 598–609
[63] Negel J-P, Voss A, Ahmed M A, Bauer D, Sutter D, Killi A and Graf T 2013 1.1 kW average output power from a thin-disk multipass amplifier for ultrashort laser pulses Opt. Lett. 38 5442–5
[64] Teisset C Y et al 2018 Multi-kW thin-disk amplifiers High-Brightness Sources and Light-Driven Interactions (Optical Society of America) p HT1A.6
[65] Ueffing M, Lange R, Pleyer T, Pervak V, Metzger T, Sutter D, Major Z, Nubbemeyer T and Krausz F 2016 Direct regenerative amplification of femtosecond pulses to the multimillijoule level Opt. Lett. 41 3840–3
[66] Russbueldt P et al 2015 Innoslab amplifiers IEEE J. Sel. Top. Quantum Electron. 21 447–63
[67] Wang Y, Chi H, Baumgarten C, Dehne K, Meadows A R, Davenport A, Murray G, Reagan B A, Menoni C S and Rocca J J 2020 1.1 J Yb:YAG picosecond laser at 1 kHz repetition rate Opt. Lett. 45 6615–8
[68] Nagy T, Simon P and Veisz L 2021 High-energy few-cycle pulses: post-compression techniques Adv. Phys. X 6 1845795
[69] Siegman A E 1986 Lasers (Mill Valley, CA: University Science Books)
[70] Böhle F et al 2014 Compression of CEP-stable multi-mJ laser pulses down to 4 fs in long hollow fibers Laser Phys. Lett. 11 095401
[71] Nagy T, Kretschmar M, Vrakking M J J and Rouzée A 2020 Generation of above-terawatt 1.5-cycle visible pulses at 1 kHz by post-compression in a hollow fiber Opt. Lett. 45 3313–6
[72] Suda A, Hatayama M, Nagasaka K and Midorikawa K 2005 Generation of sub-10-fs, 5-mJ-optical pulses using a hollow fiber with a pressure gradient Appl. Phys. Lett. 86 111116
[73] Witting T, Frank F, Arrell C A, Okell W A, Marangos J P and Tisch J W G 2011 Characterization of high-intensity sub-4-fs laser pulses using spatially encoded spectral shearing interferometry Opt. Lett. 36 1680–2
[74] Nagy T et al 2019 Generation of three-cycle multi-millijoule laser pulses at 318 W average power Optica 6 1423–4

[75] Shestaev E et al 2020 High-power ytterbium-doped fiber laser delivering few-cycle, carrier-envelope phase-stable 100 μJ pulses at 100 kHz Opt. Lett. 45 97–100
[76] Kühn S et al 2017 The ELI-ALPS facility: the next generation of attosecond sources J. Phys. B: At. Mol. Opt. Phys. 50 132002
[77] Shestaev E et al 2020 Carrier-envelope offset stable, coherently combined ytterbium-doped fiber CPA delivering 1 kW of average power Opt. Lett. 45 6350–3
[78] Hammerland D et al 2019 Reconstruction of attosecond pulses in the presence of interfering dressing fields using a 100 kHz laser system at ELI-ALPS J. Phys. B 52 23LT01
[79] Hammerland D et al 2019 Effect of electron correlations on attosecond photoionization delays in the vicinity of the Cooper minima of argon (arXiv:1907.01219 [physics.atom-ph])
[80] Ye P et al 2020 Attosecond pulse generation at ELI-ALPS 100 kHz repetition rate beamline J. Phys. B: At. Mol. Opt. Phys. 53 154004
[81] Lu C-H, Tsou Y-J, Chen H-Y, Chen B-H, Cheng Y-C, Yang S-D, Chen M-C, Hsu C-C and Kung A H 2014 Generation of intense supercontinuum in condensed media Optica 1 400–6
[82] Lu C-H, Witting T, Husakou A, Vrakking M J J, Kung A H and Furch F J 2018 Sub-4 fs laser pulses at high average power and high repetition rate from an all-solid-state setup Opt. Express 26 8941–56
[83] Cheng Y-C, Lu C-H, Lin Y-Y and Kung A H 2016 Supercontinuum generation in a multi-plate medium Opt. Express 24 7224–31
[84] He P et al 2017 High-efficiency supercontinuum generation in solid thin plates at 0.1 TW level Opt. Lett. 42 474–7
[85] Seo M, Tsendsuren K, Mitra S, Kling M and Kim D 2020 High-contrast, intense single-cycle pulses from an all thin-solid-plate setup Opt. Lett. 45 367–70
[86] Lu C-H, Wu W-H, Kuo S-H, Guo J-Y, Chen M-C, Yang S-D and Kung A H 2019 Greater than 50 times compression of 1030 nm Yb:KGW laser pulses to single-cycle duration Opt. Express 27 15638–48
[87] Beetar J E, Gholam-Mirzaei S and Chini M 2018 Spectral broadening and pulse compression of a 400 μJ, 20 W Yb:KGW laser using a multi-plate medium Appl. Phys. Lett. 112 051102
[88] Schulte J, Sartorius T, Weitenberg J, Vernaleken A and Russbueldt P 2016 Nonlinear pulse compression in a multi-pass cell Opt. Lett. 41 4511–4
[89] Hanna M, Délen X, Lavenu L, Guichard F, Zaouter Y, Druon F and Georges P 2017 Nonlinear temporal compression in multipass cells: theory J. Opt. Soc. Am. B 34 1340–7
[90] Weitenberg J, Saule T, Schulte J and Russbüldt P 2017 Nonlinear pulse compression to sub-40 fs at 4.5 μJ pulse energy by multi-pass-cell spectral broadening IEEE J. Quantum Electron. 53 8600204
[91] Lavenu L, Natile M, Guichard F, Zaouter Y, Delen X, Hanna M, Mottay E and Georges P 2018 Nonlinear pulse compression based on a gas-filled multipass cell Opt. Lett. 43 2252–5
[92] Ueffing M, Reiger S, Kaumanns M, Pervak V, Trubetskov M, Nubbemeyer T and Krausz F 2018 Nonlinear pulse compression in a gas-filled multipass cell Opt. Lett. 43 2070–3
[93] Jargot G, Daher N, Lavenu L, Delen X, Forget N, Hanna M and Georges P 2018 Self-compression in a multipass cell Opt. Lett. 43 5643–6
[94] Fritsch K, Poetzlberger M, Pervak V, Brons J and Pronin O 2018 All-solid-state multipass spectral broadening to sub-20 fs Opt. Lett. 43 4643–6
[95] Tsai C-L, Meyer F, Omar A, Wang Y, Liang A-Y, Lu C-H, Hoffmann M, Yang S-D and Saraceno C J 2019 Efficient nonlinear compression of a mode-locked thin-disk oscillator to 27 fs at 98 W average power Opt. Lett. 44 4115–8
[96] Russbueldt P, Weitenberg J, Schulte J, Meyer R, Meinhardt C, Hoffmann H D and Poprawe R 2019 Scalable 30 fs laser source with 530 W average power Opt. Lett. 44 5222–5
[97] Grebing C, Müller M, Buldt J, Stark H and Limpert J 2020 Kilowatt-average-power compression of millijoule pulses in a gas-filled multi-pass cell Opt. Lett. 45 6250–3
[98] Kaumanns M, Pervak V, Kormin D, Leshchenko V, Kessel A, Ueffing M, Chen Y and Nubbemeyer T 2018 Multipass spectral broadening of 18 mJ pulses compressible from 1.3 ps to 41 fs Opt. Lett. 43 5877–80
[99] Kaumanns M, Kormin D, Nubbemeyer T, Pervak V and Karsch S 2021 Spectral broadening of 112 mJ, 1.3 ps pulses at 5 kHz in a LG10 multipass cell with compressibility to 37 fs Opt. Lett. 46 929–32
[100] Balla P et al 2020 Postcompression of picosecond pulses into the few-cycle regime Opt. Lett. 45 2572–5
[101] Müller M, Buldt J, Stark H, Grebing C and Limpert J 2021 Multipass cell for high-power few-cycle compression Opt. Lett. 46 2678–81
[102] Hädrich S et al 2022 Carrier-envelope phase stable few-cycle laser system delivering more than 100 W, 1 mJ, sub-2-cycle pulses Opt. Lett. 47 1537–40
[103] Cao H, Nagymihaly R S, Chvykov V, Khodakovskiy N and Kalashnikov M 2019 Multipass-cell-based post-compression of radially and azimuthally polarized pulses to the sub-two-cycle regime J. Opt. Soc. Am. B 36 2517–25
[104] Cao H, Nagymihaly R S and Kalashnikov M 2020 Relativistic near-single-cycle optical vortex pulses from noble gas-filled multipass cells Opt. Lett. 45 3240–3
[105] Rueda P, Videla F, Witting T, Torchia G A and Furch F J 2021 8 fs laser pulses from a compact gas-filled multi-pass cell Opt. Express 29 27004–13
[106] Daniault L, Cheng Z, Kaur J, Hergott J-F, Réau F, Tcherbakoff O, Daher N, Délen X, Hanna M and Lopez-Martens R 2021 Single-stage few-cycle nonlinear compression of millijoule energy Ti:Sa femtosecond pulses in a multipass cell Opt. Lett. 46 5264–7
[107] Viotti A-L, Seidel M, Escoto E, Rajhans S, Leemans W P, Hartl I and Heyl C M 2022 Multi-pass cells for post-compression of ultrashort laser pulses Optica 9 197–216
[108] Lavenu L, Natile M, Guichard F, Délen X, Hanna M, Zaouter Y and Georges P 2019 High-power two-cycle ultrafast source based on hybrid nonlinear compression Opt. Express 27 1958–67
[109] Natile M et al 2019 CEP-stable high-energy ytterbium-doped fiber amplifier Opt. Lett. 44 3909–12
[110] Gaida C, Gebhardt M, Heuermann T, Stutzki F, Jauregui C and Limpert J 2018 Ultrafast thulium fiber laser system emitting more than 1 kW of average power Opt. Lett. 43 5853–6
[111] Gaida C, Stutzki F, Gebhardt M, Heuermann T, Breitkopf S, Eidam T, Rothhardt J and Limpert J 2020 4-channel coherently combined long-term-stable ultrafast thulium-doped fiber CPA Laser Congress 2020 (ASSL, LAC) (Optical Society of America) p AW5A.1
[112] Gebhardt M et al 2021 Bright, high-repetition-rate water window soft x-ray source enabled by nonlinear pulse self-compression in an antiresonant hollow-core fibre Light: Sci. Appl. 10 36

[113] Akhmanov S A, Kovrigin A I, Piskarskas A S, Fadeev V V and Khokhlov R V 1965 Observation of parametric amplification in the optical range *JETP Lett.* **2** 191
[114] Dubietis A, Jonušauskas G and Piskarskas A 1992 Powerful femtosecond pulse generation by chirped and stretched pulse parametric amplification in BBO crystal *Opt. Commun.* **88** 437–40
[115] Di Trapani P, Andreoni A, Foggi P, Solcia C, Danielius R and Piskarskas A 1995 Efficient conversion of femtosecond blue pulses by travelling-wave parametric generation in non-collinear phase matching *Opt. Commun.* **119** 327–32
[116] Boyd R W 2003 *Nonlinear Optics* (New York: Academic)
[117] Cerullo G and De Silvestri S 2003 Ultrafast optical parametric amplifiers *Rev. Sci. Instrum.* **74** 1–18
[118] Schimpf D N, Rothhardt J, Limpert J, Tünnermann A and Hanna D C 2007 Theoretical analysis of the gain bandwidth for noncollinear parametric amplification of ultrafast pulses *J. Opt. Soc. Am.* B **24** 2837–46
[119] Ross I N, Matousek P, New G H C and Osvay K 2002 Analysis and optimization of optical parametric chirped pulse amplification *J. Opt. Soc. Am.* B **19** 2945–56
[120] Rodwell M J W, Bloom D M and Weingarten K J 1989 Subpicosecond laser timing stabilization *IEEE J. Quantum Electron.* **25** 817–27
[121] Witte S, Zinkstok R T, Wolf A L, Hogervorst W, Ubachs W and Eikema K S E 2006 A source of 2 terawatt, 2.7 cycle laser pulses based on noncollinear optical parametric chirped pulse amplification *Opt. Express* **14** 8168–77
[122] Ishii N *et al* 2005 Multimillijoule chirped parametric amplification of few-cycle pulses *Opt. Lett.* **30** 567–9
[123] Teisset C Y, Ishii N, Fuji T, Metzger T, Köhler S, Holzwarth R, Baltuška A, Zheltikov A M and Krausz F 2005 Soliton-based pump-seed synchronization for few-cycle OPCPA *Opt. Express* **13** 6550–7
[124] Nillon J, Montant S, Boullet J, Desmarchelier R, Zaouter Y, Cormier E and Petit S 2009 15-fs, 1-μJ, 100-kHz pulses by direct seeding of a NOPA and its fiber pump by a CEP stabilized Ti:Sapphire oscillator *2009 Conf. on Lasers and Electro-Optics and 2009 Conf. on Quantum Electronics and Laser Science Conf.* pp 1–2
[125] Schultze M, Binhammer T, Palmer G, Emons M, Lang T and Morgner U 2010 Multi-μJ, CEP-stabilized, two-cycle pulses from an OPCPA system with up to 500 kHz repetition rate *Opt. Express* **18** 27291–7
[126] Furch F J, Birkner S, Kelkensberg F, Giree A, Anderson A, Schulz C P and Vrakking M J J 2013 Carrier-envelope phase stable few-cycle pulses at 400 kHz for electron-ion coincidence experiments *Opt. Express* **21** 22671–82
[127] Furch F J, Giree A, Morales F, Anderson A, Wang Y, Schulz C P and Vrakking M J J 2016 Close to transform-limited, few-cycle 12 μJ pulses at 400 kHz for applications in ultrafast spectroscopy *Opt. Express* **24** 19293–310
[128] Matyschok J *et al* 2013 Temporal and spatial effects inside a compact and CEP stabilized, few-cycle OPCPA system at high repetition rates *Opt. Express* **21** 29656–65
[129] Rothhardt J, Demmler S, Hädrich S, Limpert J and Tünnermann A 2012 Octave-spanning OPCPA system delivering CEP-stable few-cycle pulses and 22 W of average power at 1 MHz repetition rate *Opt. Express* **20** 10870–8
[130] Prinz S *et al* 2015 CEP-stable, sub-6 fs, 300-kHz OPCPA system with more than 15 W of average power *Opt. Express* **23** 1388–94
[131] Hrisafov S, Pupeikis J, Chevreuil P-A, Brunner F, Phillips C R, Gallmann L and Keller U 2020 High-power few-cycle near-infrared OPCPA for soft x-ray generation at 100 kHz *Opt. Express* **28** 40145–54
[132] Furch F J, Witting T, Giree A, Luan C, Schell F, Arisholm G, Schulz C P and Vrakking M J J 2017 CEP-stable few-cycle pulses with more than 190 μJ of energy at 100 kHz from a noncollinear optical parametric amplifier *Opt. Lett.* **42** 2495–8
[133] Witting T, Furch F J and Vrakking M J J 2018 Spatio-temporal characterisation of a 100 kHz 24 W sub-3-cycle NOPCPA laser system *J. Opt.* **20** 044003
[134] Furch F J, Witting T, Osolodkov M, Schell F, Schulz C P and Vrakking M J J 2019 High-repetition rate optical parametric chirped pulse amplification system for attosecond science experiments *Proc. SPIE* **11034** 110340I
[135] Harth A, Schultze M, Lang T, Binhammer T, Rausch S and Morgner U 2012 Two-color pumped OPCPA system emitting spectra spanning 1.5 octaves from VIS to NIR *Opt. Express* **20** 3076–81
[136] Schulz M *et al* 2011 Yb:YAG Innoslab amplifier: efficient high repetition rate subpicosecond pumping system for optical parametric chirped pulse amplification *Opt. Lett.* **36** 2456–8
[137] Dubietis A, Tamošauskas G, Šuminas R, Jukna V and Couairon A 2017 Ultrafast supercontinuum generation in bulk condensed media *Lith. J. Phys.* **57**
[138] Mücke O D *et al* 2009 Scalable Yb-MOPA-driven carrier-envelope phase-stable few-cycle parametric amplifier at 1.5 μm *Opt. Lett.* **34** 118–20
[139] Budriūnas R, Stanislauskas T and Varanavičius A 2015 Passively CEP-stabilized frontend for few cycle terawatt OPCPA system *J. Opt.* **17** 094008
[140] Fattahi H *et al* 2014 Third-generation femtosecond technology *Optica* **1** 45–63
[141] Mecseki K, Windeler M K R, Miahnahri A, Robinson J S, Fraser J M, Fry A R and Tavella F 2019 High average power 88 W OPCPA system for high-repetition-rate experiments at the LCLS x-ray free-electron laser *Opt. Lett.* **44** 1257–60
[142] Shamir Y, Rothhardt J, Hädrich S, Demmler S, Tschernajew M, Limpert J and Tünnermann A 2015 High-average-power 2 μm few-cycle optical parametric chirped pulse amplifier at 100 kHz repetition rate *Opt. Lett.* **40** 5546–9
[143] Mero M, Heiner Z, Petrov V, Rottke H, Branchi F, Thomas G M and Vrakking M J J 2018 43 W, 1.55 μm and 12.5 W, 3.1 μm dual-beam, sub-10 cycle, 100 kHz optical parametric chirped pulse amplifier *Opt. Lett.* **43** 5246–9
[144] Thiré N *et al* 2018 Highly stable, 15 W, few-cycle, 65 mrad CEP-noise mid-IR OPCPA for statistical physics *Opt. Express* **26** 26907–15
[145] Neuhaus M *et al* 2018 10 W CEP-stable few-cycle source at 2 μm with 100 kHz repetition rate *Opt. Express* **26** 16074–85
[146] Bigler N, Pupeikis J, Hrisafov S, Gallmann L, Phillips C R and Keller U 2018 High-power OPCPA generating 1.7 cycle pulses at 2.5 μm *Opt. Express* **26** 26750–7
[147] Rigaud P, Van de Walle A, Hanna M, Forget N, Guichard F, Zaouter Y, Guesmi K, Druon F and Georges P 2016 Supercontinuum-seeded few-cycle mid-infrared OPCPA system *Opt. Express* **24** 26494–502
[148] Baudisch M, Wolter B, Pullen M, Hemmer M and Biegert J 2016 High power multi-color OPCPA source with simultaneous femtosecond deep-UV to mid-IR outputs *Opt. Lett.* **41** 3583–6
[149] Windeler M K R, Mecseki K, Miahnahri A, Robinson J S, Fraser J M, Fry A R and Tavella F 2019 100 W high-repetition-rate near-infrared optical parametric chirped pulse amplifier *Opt. Lett.* **44** 4287–90
[150] Elu U, Baudisch M, Pires H, Tani F, Frosz M H, Köttig F, Ermolov A, Russell P S J and Biegert J 2017 High average power and single-cycle pulses from a mid-IR optical parametric chirped pulse amplifier *Optica* **4** 1024–9

[151] Popmintchev T et al 2012 Bright coherent ultrahigh harmonics in the keV x-ray regime from mid-infrared femtosecond lasers Science 336 1287–91
[152] Colosimo P et al 2008 Scaling strong-field interactions towards the classical limit Nat. Phys. 4 386–9
[153] Pupeikis J, Chevreuil P-A, Bigler N, Gallmann L, Phillips C R and Keller U 2020 Water window soft x-ray source enabled by a 25 W few-cycle 2.2 μm OPCPA at 100 kHz Optica 7 168–71
[154] Meckel M et al 2008 Laser-induced electron tunneling and diffraction Science 320 1478–82
[155] Riedel R et al 2014 Thermal properties of borate crystals for high power optical parametric chirped-pulse amplification Opt. Express 22 17607–19
[156] Riedel R, Stephanides A, Prandolini M J, Gronloh B, Jungbluth B, Mans T and Tavella F 2014 Power scaling of supercontinuum seeded megahertz-repetition rate optical parametric chirped pulse amplifiers Opt. Lett. 39 1422–4
[157] Baudisch M, Hemmer M, Pires H and Biegert J 2014 Performance of MgO:PPLN, KTA, and $KNbO_3$ for mid-wave infrared broadband parametric amplification at high average power Opt. Lett. 39 5802–5
[158] Budriūnas R, Stanislauskas T, Adamonis J, Aleknavičius A, Veitas G, Gadonas D, Balickas S, Michailovas A and Varanavičius A 2017 53 W average power CEP-stabilized OPCPA system delivering 5.5 TW few cycle pulses at 1 kHz repetition rate Opt. Express 25 5797–806
[159] Xu L et al 2013 High-energy noncollinear optical parametric chirped pulse amplification in LBO at 800 nm Opt. Lett. 38 4837–40
[160] Zhang Q, Takahashi E J, Mücke O D, Lu P and Midorikawa K 2011 Dual-chirped optical parametric amplification for generating few hundred mJ infrared pulses Opt. Express 19 7190–212
[161] Fu Y, Midorikawa K and Takahashi E J 2018 Towards a petawatt-class few-cycle infrared laser system via dual-chirped optical parametric amplification Sci. Rep. 8 7692
[162] Schibli T R, Kim J, Kuzucu O, Gopinath J T, Tandon S N, Petrich G S, Kolodziejski L A, Fujimoto J G, Ippen E P and Kaertner F X 2003 Attosecond active synchronization of passively mode-locked lasers by balanced cross correlation Opt. Lett. 28 947–9
[163] Schwarz A, Ueffing M, Deng Y, Gu X, Fattahi H, Metzger T, Ossiander M, Krausz F and Kienberger R 2012 Active stabilization for optically synchronized optical parametric chirped pulse amplification Opt. Express 20 5557–65
[164] Hädrich S, Rothhardt J, Krebs M, Demmler S, Limpert J and Tünnermann A 2012 Improving carrier-envelope phase stability in optical parametric chirped-pulse amplifiers by control of timing jitter Opt. Lett. 37 4910–2
[165] Prinz S, Häfner M, Schultze M, Teisset C Y, Bessing R, Michel K, Kienberger R and Metzger T 2014 Active pump-seed-pulse synchronization for OPCPA with sub-2-fs residual timing jitter Opt. Express 22 31050–6
[166] Bromage J, Rothhardt J, Hädrich S, Dorrer C, Jocher C, Demmler S, Limpert J, Tünnermann A and Zuegel J D 2011 Analysis and suppression of parasitic processes in noncollinear optical parametric amplifiers Opt. Express 19 16797–808
[167] Giree A, Mero M, Arisholm G, Vrakking M J J and Furch F J 2017 Numerical study of spatiotemporal distortions in noncollinear optical parametric chirped-pulse amplifiers Opt. Express 25 3104–21
[168] Austin D R, Witting T and Walmsley I A 2009 High precision self-referenced phase retrieval of complex pulses with multiple-shearing spectral interferometry J. Opt. Soc. Am. B 26 1818–30
[169] Bromage J, Dorrer C and Zuegel J D 2010 Angular-dispersion-induced spatiotemporal aberrations in noncollinear optical parametric amplifiers Opt. Lett. 35 2251–3
[170] Zaukevičius A, Jukna V, Antipenkov R, Martinėnaitė V, Varanavičius A, Piskarskas A P and Valiulis G 2011 Manifestation of spatial chirp in femtosecond noncollinear optical parametric chirped-pulse amplifier J. Opt. Soc. Am. B 28 2902–8
[171] Gabolde P, Lee D, Akturk S and Trebino R 2007 Describing first-order spatio-temporal distortions in ultrashort pulses using normalized parameters Opt. Express 15 242–51
[172] Kakehata M, Takada H, Kobayashi Y, Torizuka K, Fujihira Y, Homma T and Takahashi H 2001 Single-shot measurement of carrier-envelope phase changes by spectral interferometry Opt. Lett. 26 1436–8
[173] Wittmann T, Horvath B, Helml W, Schätzel M G, Gu X, Cavalieri A L, Paulus G G and Kienberger R 2009 Single-shot carrier-envelope phase measurement of few-cycle laser pulses Nat. Phys. 5 357–62
[174] Becker W, Grasbon F, Kopold R, Milošević D B, Paulus G G and Walther H 2002 Above-threshold ionization: from classical features to quantum effects Advances in Atomic, Molecular and Optical Physics vol 48 (New York: Academic) pp 35–98
[175] Hoff D, Furch F J, Witting T, Rühle K, Adolph D, Max Sayler A, Vrakking M J J, Paulus G G and Schulz C P 2018 Continuous every-single-shot carrier-envelope phase measurement and control at 100 kHz Opt. Lett. 43 3850–3
[176] Witting T et al 2022 Generation and characterization of isolated attosecond pulses at 100 kHz repetition rate Optica 9 145–51
[177] Hädrich S, Rothhardt J, Krebs M, Demmler S, Klenke A, Tünnermann A and Limpert J 2016 Single-pass high harmonic generation at high repetition rate and photon flux J. Phys. B: At. Mol. Opt. Phys. 49 172002
[178] Rothhardt J, Krebs M, Hädrich S, Demmler S, Limpert J and Tünnermann A 2014 Absorption-limited and phase-matched high harmonic generation in the tight focusing regime New J. Phys. 16 033022
[179] Heyl C M, Arnold C L, Couairon A and L'Huillier A 2016 Introduction to macroscopic power scaling principles for high-order harmonic generation J. Phys. B: At. Mol. Opt. Phys. 50 013001
[180] Krebs M, Hädrich S, Demmler S, Rothhardt J, Zaïr A, Chipperfield L, Limpert J and Tünnermann A 2013 Towards isolated attosecond pulses at megahertz repetition rates Nat. Photon. Lett. 7 555–9
[181] Harth A et al 2017 Compact 200 kHz HHG source driven by a few-cycle OPCPA J. Opt. 20 014007
[182] Gonzalez A I et al 2018 Spatio-spectral structures in high harmonic generation driven by tightly focused high repetition rate lasers J. Opt. Soc. Am. B 35 A6–A14
[183] Lorek E, Larsen E W, Heyl C M, Carlstrom S, Palecek D, Zigmantas D and Mauritsson J 2014 High-order harmonic generation using a high-repetition-rate turnkey laser Rev. Sci. Instrum. 85 123106
[184] Hädrich S, Klenke A, Rothhardt J, Krebs M, Hoffmann A, Pronin O, Pervak V, Limpert J and Tünnermann A 2014 High photon flux table-top coherent extreme-ultraviolet source Nat. Photon. 8 779–83
[185] Comby A, Descamps D, Beauvarlet S, Gonzalez A, Guichard F, Petit S, Zaouter Y and Mairesse Y 2019 Cascaded harmonic generation from a fiber laser: a milliwatt XUV source Opt. Express 27 20383–96
[186] Rudawski P et al 2015 Carrier-envelope phase dependent high-order harmonic generation with a high-repetition rate OPCPA-system Eur. Phys. J. D 69 70
[187] Puppin M et al 2019 Time- and angle-resolved photoemission spectroscopy of solids in the extreme ultraviolet at 500 kHz repetition rate Rev. Sci. Instrum. 90 023104
[188] Zürch M, Rothhardt J, Hädrich S, Demmler S, Krebs M, Limpert J, Tünnermann A, Guggenmos A, Kleineberg U and Spielmann C 2014 Real-time and sub-wavelength ultrafast coherent diffraction imaging in the extreme ultraviolet Sci. Rep. 5 7356

[189] Rothhardt J et al 2016 High-repetition-rate and high-photon-flux 70 eV high-harmonic source for coincidence ion imaging of gas-phase molecules Opt. Express 24 18133–47
[190] Cheng Y-C et al 2020 Controlling photoionization using attosecond time-slit interferences Proc. Natl Acad. Sci. 117 10727–32
[191] Srinivas H, Shobeiryt F, Bharti D, Harth A, Pfeifer T and Moshammer R 2020 Angle-resolved time delays in photoionization with a high repetition rate laser source J. Phys.: Conf. Ser. 1412 072033
[192] Mikaelsson S et al 2021 A high-repetition rate attosecond light source for time-resolved coincidence spectroscopy Nanophotonics 10 117–28
[193] Srinivas H, Shobeiry F, Bharti D, Pfeifer T, Moshammer R and Harth A 2022 High-repetition rate attosecond beamline for multi-particle coincidence experiments Opt. Express 30 13630–46
[194] López-Martens R et al 2005 Amplitude and phase control of attosecond light pulses Phys. Rev. Lett. 94 033001
[195] Osolodkov M, Furch F J, Schell F, Šušnjar P, Cavalcante F, Menoni C S, Schulz C P, Witting T and Vrakking M J J 2020 Generation and characterisation of few-pulse attosecond pulse trains at 100 kHz repetition rate J. Phys. B: At. Mol. Opt. Phys. 53 194003
[196] Ghafur O, Siu W, Johnsson P, Kling M F, Drescher M and Vrakking M J J 2009 A velocity map imaging detector with an integrated gas injection system Rev. Sci. Instrum. 80 033110
[197] Itatani J, Quéré F, Yudin G L, Ivanov M Y, Krausz F and Corkum P B 2002 Attosecond streak camera Phys. Rev. Lett. 88 173903
[198] Trebino R 2000 Frequency-Resolved Optical Gating (Berlin: Springer)
[199] Mairesse Y and Quéré F 2005 Frequency-resolved optical gating for complete reconstruction of attosecond bursts Phys. Rev. A 71 011401
[200] Ratner J, Steinmeyer G, Wong T C, Bartels R and Trebino R 2012 Coherent artifact in modern pulse measurements Opt. Lett. 37 2874–6
[201] Witting T, Furch F J, Kornilov O, Osolodkov M, Schulz C P and Vrakking M J J 2020 Retrieval of attosecond pulse ensembles from streaking experiments using mixed state time-domain ptychography J. Phys. B: At. Mol. Opt. Phys. 53 194001
[202] Goulielmakis E et al 2004 Direct measurement of light waves Science 305 1267–9
[203] Keathley P D, Bhardwaj S, Moses J, Laurent G and Kärtner F X 2016 Volkov transform generalized projection algorithm for attosecond pulse characterization New J. Phys. 18 073009
[204] Birkner S 2015 Strong field ionization of atoms and molecules: electron-ioncoincidence measurements at high repetition rate Doctoral Dissertation Freie Universität Berlin
[205] Schell F 2020 Sub-femtosecond processes in molecules studied by coincidence spectroscopy Doctoral Dissertation Freie Universität Berlin
[206] Cirelli C et al 2018 Anisotropic photoemission time delays close to a Fano resonance Nat. Commun. 9 955
[207] Nisoli M, Decleva P, Calegari F, Palacios A and Martín F 2017 Attosecond electron dynamics in molecules Chem. Rev. 117 10760–825
[208] Carlström S, Mauritsson J, Schafer K J, L'Huillier A and Gisselbrecht M 2017 Quantum coherence in photo-ionisation with tailored XUV pulses J. Phys. B: At. Mol. Opt. Phys. 51 015201
[209] Bourassin-Bouchet C, Barreau L, Gruson V, Hergott J-F, Quéré F, Salières P and Ruchon T 2020 Quantifying decoherence in attosecond metrology Phys. Rev. X 10 031048
[210] Vrakking M J J 2021 Control of attosecond entanglement and coherence Phys. Rev. Lett. 126 113203
[211] Koll L-M, Maikowski L, Drescher L, Witting T and Vrakking M J J 2022 Experimental control of quantum-mechanical entanglement in an attosecond pump-probe experiment Phys. Rev. Lett. 128 043201
[212] Nishi T, Lötstedt E and Yamanouchi K 2019 Entanglement and coherence in photoionization of H_2 by an ultrashort XUV laser pulse Phys. Rev. A 100 013421
[213] Galli M et al 2019 Generation of deep ultraviolet sub-2-fs pulses Opt. Lett. 44 1308–11
[214] Palacios A and Martín F 2020 The quantum chemistry of attosecond molecular science Wiley Interdiscip. Rev.-Comput. Mol. Sci. 10 e1430